
1 **Distinctive aerosol-cloud-precipitation interactions in marine boundary layer clouds from the**
2 **ACE-ENA and SOCRATES aircraft field campaigns**

3
4 Xiaojian Zheng^{1,a}, Xiquan Dong¹, Baike Xi¹, Timothy Logan² and Yuan Wang³

5
6 ¹Department of Hydrology and Atmospheric Sciences, University of Arizona, Tucson, AZ, USA

7 ²Department of Atmospheric Sciences, Texas A&M University, College Station, TX, USA

8 ³Department of Earth System Sciences, Stanford University, Stanford, CA, USA

9 ^aNow at: Environmental Science Division, Argonne National Laboratory, Lemont, IL, USA

10
11 **Correspondence:** Xiquan Dong (xdong@arizona.edu)

12
13 **Abstract.** The aerosol-cloud-precipitation interactions within the cloud-topped Marine Boundary Layer
14 (MBL) are being examined using aircraft in-situ measurements from Aerosol and Cloud Experiments in
15 the Eastern North Atlantic (ACE-ENA) and Southern Ocean Clouds Radiation Aerosol Transport
16 Experimental Study (SOCRATES) field campaigns. SOCRATES clouds have a larger number and
17 smaller cloud droplets (148.3 cm⁻³ and 8.0 μm) compared to ACE-ENA summertime (89.4 cm⁻³ and 9.0
18 μm) and wintertime clouds (70.6 cm⁻³ and 9.8 μm). The ACE-ENA clouds, especially in wintertime,
19 exhibit stronger drizzle formation and growth due to enhanced collision-coalescence, attributed to the
20 relatively cleaner environment and deeper cloud layer. Furthermore, the Aerosol-Cloud Interaction (ACI)
21 indices from the two aircraft field campaigns suggest distinct sensitivities, indicating the cloud
22 microphysical responses to aerosols reside in different regimes. Aerosols during ACE-ENA winter are
23 more likely to be activated into cloud droplets under sufficient water availability and strong turbulence,
24 given the aerosol-limited regime. The enriched aerosol loading during ACE-ENA summer and
25 SOCRATES generally leads to smaller cloud droplets competing for available water vapor and exhibiting

Deleted:),

Deleted: (148.3 cm⁻³)

Deleted: μm

Deleted: cm⁻³

Deleted: μm

Deleted: cm⁻³

Deleted: μm

33 a stronger ACI in the water-vapor-limit regime. Notably, the precipitation susceptibilities are more
34 pronounced during the ACE-ENA than during the SOCRATES campaigns. The in-cloud drizzle
35 evolutions significantly alter sub-cloud cloud condensation nuclei (CCN) budgets through the
36 coalescence-scavenging effect, and in turn, impact the ACI assessments. The results of this study can
37 enhance the understanding and aid in future model simulation and assessment of the aerosol-cloud
38 interaction.

39
40

41 **1. Introduction**

42 Marine boundary layer (MBL) clouds substantially impact the Earth's climate system (Dong and
43 Minnis, 2022). Sustained by large-scale subsidence and cloud-top longwave radiative cooling, MBL
44 clouds, typically located beneath the temperature inversion at the MBL top, persistently reflect the
45 incoming solar radiation and modulate the radiative balance (Lilly, 1968; Albrecht et al., 1995; Wood et
46 al., 2015; Dong et al., 2023). The climatic significance of MBL cloud radiative effects, which remains
47 largely uncertain (IPCC, 2022), is closely linked to cloud microphysical properties that are substantially
48 influenced by surrounding aerosol conditions (Chen et al., 2014; Feingold and McComiskey, 2016).
49 Observational evidence demonstrates that cloud microphysical responses to aerosols, defined as the
50 aerosol-cloud interaction (ACI), can be typically viewed as decreased cloud droplet effective radii (r_c)
51 and increased number concentrations (N_c) with more aerosol intrusion, under conditions of comparable
52 cloud water content (Feingold and McComiskey, 2016). The ACIs have been extensively investigated
53 by different observational platforms, such as aircraft (Hill et al., 2009; Diamond et al., 2018; Gupta et
54 al., 2022), ground-based and satellite observations (Painemal et al., 2020; Zhang et al., 2022; Zheng et
55 al., 2022a), and model simulations (Wang et al., 2020; Christensen et al., 2023) over different maritime
56 regions like the southeast Pacific (Painemal and Zuidema, 2011), northeast Pacific (Braun et al., 2018),
57 southeast Atlantic (Gupta et al., 2022), and eastern North Atlantic (Zheng et al., 2022a).

Deleted: ,

59 Furthermore, more and smaller cloud droplets not only extend cloud longevity and spatial
60 coverage but also modulate the precipitation processes, reflecting the cloud adjustments to aerosol
61 disturbances (Albrecht, 1989; Bellouin et al., 2020). Precipitation, particularly in the form of drizzle, is
62 common in MBL clouds (Wood et al., 2015; Wu et al., 2020), and the turbulence forced by stratocumulus
63 cloud-top radiative cooling can increase the cloud liquid water path, and contribute to drizzle production
64 (Ghate et al., 2019, 2021). The drizzle formation and growth processes are deeply entwined with the
65 MBL aerosols and dynamics. Aerosols have been found to suppress the precipitation frequency and
66 strength by constantly buffering cloud droplet number concentrations via activation, hence increasing
67 cloud precipitation susceptibility (Feingold and Seibert, 2009; Lu et al., 2009; Sorooshian et al., 2009;
68 Duong et al., 2011). Furthermore, the assessments of precipitation susceptibility are examined to be under
69 the influences of methodology (Terai et al., 2012), cloud morphology (Sorooshian et al., 2009; Jung et
70 al., 2016), ambient aerosol concentrations (Duong et al., 2011; Jung et al., 2016; Gupta et al., 2022), and
71 cloud thickness (Terai et al., 2012; Jung et al., 2016; Gupta et al., 2022). The in-cloud turbulence and
72 wind shear can effectively enhance collision-coalescence efficiency, stimulating drizzle formation and
73 growth, and consequently leading to enhanced precipitation (Chen et al., 2011; Wu et al., 2017). Cloud-
74 top entrainment of dryer and warmer air can potentially deplete small cloud droplets and shrink large
75 droplets via evaporation, thereby impacting cloud top microphysical processes depending on the
76 homogeneous or inhomogeneous mixing regimes (Lehmann et al., 2009; Jia et al., 2019).

77 Conversely, precipitation has been shown to exert a substantial influence on the MBL aerosol and
78 cloud condensation nuclei (CCN) budget through the coalescence-scavenging effect. The coalescence-
79 scavenging refers to the process in which cloud or drizzle droplets, containing aerosol particles inside,
80 merge with each other. Upon the collision-coalescence of cloud droplets, the dissolved aerosol masses
81 within the cloud droplets also collide and merge into a larger aerosol core, leading to larger aerosol
82 particles upon droplet evaporation. The sub-cloud aerosols are then replenished into the cloud layer,
83 experiencing growth within the cloud through cloud and drizzle droplet collision-coalescence, and

Deleted: ,

Deleted: ,

86 subsequently falling and evaporating outside the cloud again. Eventually, the residual aerosols
87 undergoing this cloud-processing cycle will gradually decrease in number concentration and increase in
88 size (Flossmann et al., 1985; Feingold et al., 1996; Hudson and Noble, 2020; Hoffmann and Feingold,
89 2023). In addition, the drizzle drops, once falling out of the cloud base, can result in net reductions in
90 sub-cloud aerosols and CCN budgets also via the precipitation scavenging processes (Wood, 2006;
91 Zheng et al., 2022b). Quantitative estimates of these effects remain ambiguous and inconclusive, which
92 are subject to multiple factors such as aerosol physicochemical characteristics, cloud morphology, and
93 MBL dynamics and thermodynamics conditions (Sorooshian et al., 2009; Duong et al., 2011; Diamond
94 et al., 2018; Brunke et al., 2022). Thus, more studies on the aforementioned processes regarding MBL
95 aerosols and clouds over different maritime regions are warranted to pursue an in-depth understanding
96 of aerosol-cloud-precipitation interactions (ACPIs).

97 The Eastern North Atlantic (ENA) stands as a desirable region for exploring MBL clouds in the
98 mid-latitude, with Graciosa Island in the Azores (39.09°N, 28.03°W) representing a focal point for such
99 studies. Located between the mid-latitude and subtropical climate zones, Graciosa is subject to the
100 meteorological influence of both the Icelandic Low and the Azores High, and the influence of aerosols
101 ranging from pristine marine air masses to those heavily influenced by continental emissions from North
102 America and Northern Europe (Logan et al., 2014; Wood et al., 2015; Wang et al., 2020). Addressing
103 the need for sustained research into the MBL clouds, the recent Aerosol and Cloud Experiments in the
104 Eastern North Atlantic (ACE-ENA) aircraft campaign (J. Wang et al., 2022) were conducted in the
105 summer (June and July) 2017 ([ACE-ENA Sum](#)) and winter (January and February) 2018 ([ACE-ENA](#)
106 Win). During these two intensive operation periods (IOPs) of ACE-ENA, the research aircraft accrued
107 abundant in-situ measurements of aerosols, clouds, and drizzle properties, providing invaluable resources
108 for studying the ACI and ACPI processes. During the summer, the Azores is located at the eastern part
109 of the high-pressure system, while during the winter, the center of the Azores high shifts to the eastern
110 Atlantic and is primarily located directly over the Azores (Mechem et al., 2018; J. Wang et al., 2022).

Deleted: ACEENA

Deleted: ACEENA

113 Furthermore, both summer and winter IOPs of ACE-ENA featured ~~anomalously strong~~ high-pressure
114 systems, compared to the 20-year climatology, as shown in Figure S1. This meteorological pattern is
115 favorable to the prevailing and persistent stratocumulus clouds observed during the ACE-ENA,
116 especially for the winter IOP, where the enhanced large-scale subsidence would lead to ~~stronger and~~
117 ~~sharper temperature inversion above the~~ stratocumulus-topped MBL (Rémillard and Tselioudis, 2015;
118 Jensen et al., 2021; [Marcovecchio et al., 2022](#)). The ACE-ENA summer IOP is characterized by
119 anomalously low MBL heights and substantial MBL decoupling (Miller et al., 2021; J. Wang et al., 2022).
120 ~~The winter IOP was under the frequent impacts of the mid-latitude systems and prevalently~~ featured
121 precipitation-generated cold pools, where evaporative cooling alters the thermodynamical structure of
122 the MBL, sustains and enhances turbulence mixing, hence contributes to dynamical perturbations that
123 can influence the behavior of the MBL (Terai and Wood, 2013; Zuidema et al., 2017; Jensen et al., 2021;
124 J. Wang et al., 2022; [Smalley et al., 2024](#)). In recent years, many observational studies based on ACE-
125 ENA data have focused on the seasonal contrasts of the aerosol distributions and sources (Y. Wang et
126 al., 2021b; Zawadowicz et al., 2021), the cloud and drizzle microphysics vertical distributions (Wu et al.,
127 2020a; Zheng et al., 2022b), as well as the impacts of MBL conditions on the cloud structure and
128 morphology (Jensen et al., 2021). However, they seldom analyze the comprehensive interactions between
129 aerosol, clouds and precipitation.

130 Over the Southern Ocean (SO), the Southern Ocean Clouds Radiation Aerosol Transport
131 Experimental Study (SOCRATES) field campaign (McFarquhar et al., 2021) was conducted during the
132 austral summer (January and February 2018), which marks another valuable piece of the MBL cloud
133 research. The SO, being one of the cloudiest regions globally, is predominantly influenced by naturally
134 produced aerosols originating from oceanic sources due to its remoteness, where the anthropogenic and
135 biomass burning aerosols exert minimal influence over the region (McCoy et al., 2021; Sanchez et al.,
136 2021; Twohy et al., 2021; Zhang et al., 2023). The aerosol budget in this region is primarily shaped by
137 biological aerosols, which nucleate from the oxidation products of dimethyl sulfide (DMS) emissions, as

Deleted: are

Deleted: with anomalous stronger

Deleted: a deeper

Deleted:), while the

Deleted: is

Deleted: with prevalent

Deleted:). Over the

Deleted: ,

Deleted: the

Deleted: ,

148 well as by sea spray aerosols. Hence, the SO provides an unparalleled natural laboratory for discerning
149 the influence of these natural aerosol emissions on the MBL clouds under a pre-industrial natural
150 environment. The summertime SO region, particularly near the SOCRATES focus area, is characterized
151 by more frequently closed-cell mesoscale cellular convection structures (Danker et al., 2022; Lang et al.,
152 2022). Furthermore, the MBL clouds over the SO predominantly consist of supercooled liquid water
153 droplets, which coexist with mixed- and ice-phase processes (Y. Wang et al., 2021a; Xi et al., 2022),
154 while the precipitation phases are examined to be primarily dominated by liquid hydrometeors (Tansey
155 et al., 2022; Kang et al., 2024). The in-situ measurements collected from SOCRATES have cultivated
156 numerous studies on aerosols, clouds, and precipitation over the SO using both in-situ measurements and
157 model simulations (McCoy et al., 2020; Altas et al., 2021; D'Alessandro et al., 2021), and provides an
158 opportunity to study the liquid cloud processes under a colder nature. As shown in Figure S1c,
159 compositely speaking, the SOCRATES cloud cases used in this study are located ahead of the
160 anomalously strong thermal ridge and behind the thermal trough, providing a set up favorable to the
161 closed cellular MBL cloud structures (McCoy et al., 2017; Lang et al., 2022). The region of selected
162 SOCRATES cloud cases crosses a larger latitudinal zone and is under more consistent influence of mid-
163 latitude cyclone systems than the ACE-ENA during the summer IOP, the cloud sampling periods used
164 in this study majority reside in the closed-cell MBL stratocumulus decks.

165 The cloud cases selected from the ACE-ENA and SOCRATES share similar cloud morphology
166 (stratocumulus) while experiencing different aerosol sources and meteorological conditions. Using a
167 synergistic approach to compare data from these different field campaigns can provide valuable insights
168 to the community regarding the dominant physical processes of the interactions between aerosols, clouds,
169 and precipitation under the influence of different MBL dynamic and thermodynamic conditions. This
170 study targets the similarities and differences in the MBL aerosol, cloud, and drizzle properties, their
171 distribution and evolution, and more appealingly, the ACIs and ACPIs between the two campaigns. The
172 data and methods used in this study are introduced in section 2. The aerosol and CCN properties in the

Deleted: anomaly-stronger

Deleted: While the

Deleted: over

Deleted: region

Deleted: functioning

178 above- and sub-cloud regimes, as well as the vertical distributions of MBL cloud and drizzle properties,
179 are examined in section 3. The ACI, precipitation susceptibility and drizzle impacts on the sub-cloud
180 aerosols and CCN (ACPI) are discussed in section 4. Finally, the findings are summarized, and the
181 importance of this study is discussed in section 5.

182

183 **2. Data and methods**

184 **2.1 Cloud and drizzle properties**

185 The in-situ measurements of MBL cloud properties are temporally synchronized to 1 Hz
186 resolution, corresponding to approximately 100 m (5 m) of horizontal (vertical) sampling. The sampling
187 locations of the selected cases are indicated by the white dots in Figure S1. The Fast Cloud Droplet Probe
188 (FCDP) onboard the aircraft during ACE-ENA can detect droplets with diameter (D_p) ranging from 1.5
189 μm to 50 μm , with the size bins of the probe between 1 and 3 μm (Glienke and Mei, 2020). While the
190 SOCRATES used a similar CDP to measure droplets from 2 μm to 50 μm at a 2 μm probe size bin width.
191 Both ACE-ENA and SOCRATES leverage the Two-Dimensional Stereo Particle Imaging Probe (2DS)
192 to discern droplets with diameters from 5 μm to 1280 μm (Lawson et al., 2006; Glienke and Mei, 2019).
193 The 2DS in-situ measurements will be used as additional screening to eliminate the ice particles with
194 diameters larger than 200 μm . Moreover, the University of Washington Ice-Liquid Discriminator
195 product, which is a Machine-learning-based single-particle phase classification of the 2DS images (Atlas
196 et al., 2021), is used to identify small ice crystals when available. Through these three datasets, we can
197 tease out the ice-dominated period to the utmost extent and focus on the liquid cloud processes and ACI
198 during the SOCRATES (Wang et al., 2021).

199 Although these in-situ measurements can provide “ground-truth” datasets, their uncertainties
200 must be properly analyzed and data quality must be controlled before being applied to scientific studies.
201 The uncertainties of FCDP in sizing and concentration are approximately 30% and 20%, respectively
202 (Baumgardner et al., 2017). Considering the significant uncertainty in the concentration of smaller

203 particles from a photodiode probe such as 2DS (Baumgardner & Korolev, 1997; Wang et al., 2021), a
 204 diameter of 40 μm is used as the demarcation line between cloud droplets and drizzle drops (Wood et al.,
 205 2005). Then droplet number concentrations in the overlapping size bin between FCDP and 2DS are
 206 redistributed assuming a gamma distribution, thereby a complete size spectrum of cloud and drizzle can
 207 be merged from FCDP and 2DS measurements. Hence, the cloud and drizzle microphysical properties
 208 can be calculated.

209 The cloud droplet number concentration (N_c) is given by:

$$210 \quad N_c = \int_2^{40} n(D_p) dD_p, \quad (1)$$

211 The cloud droplet effective radius (r_c , Hansen and Travis, 1974) is given by:

$$212 \quad r_c = \frac{\int_2^{40} r_p^3 n(D_p) dD_p}{\int_2^{40} r_p^2 n(D_p) dD_p}, \quad (2)$$

213 The cloud liquid water content (LWC_c) can be calculated by:

$$214 \quad LWC_c = \frac{4}{3} \pi \rho_w \int_2^{40} D^3 n(D_p) dD_p, \quad (3)$$

215 where ρ_w is water density.

216 Similarly, the drizzle drop number concentration (N_d) and liquid water content (LWC_d) can be calculated
 217 using the size distribution from 40 μm to 1280 μm . Particularly, the drizzle mean mass diameter (D_{mmd})
 218 is given by:

$$219 \quad D_{mmd} = \left(\frac{\int_{40}^{1280} D_p^3 n(D_p) dD_p}{\int_{40}^{1280} n(D_p) dD_p} \right)^{1/3}, \quad (4)$$

220 This quantity is chosen because the D_{mmd} denotes the diameter of average mass (the third-moment
 221 average) of the drizzle size distribution, which provides the link between the number concentration and
 222 the mass concentration of drizzle droplets in a sample (Hinds, 1999).

223 Adapting the method in Zheng et al. (2022b), the cloud base precipitation rate (R_{CB}) is given by:

$$224 \quad R_{CB}(\text{mm/hr}) = 6\pi * 10^{-4} \int_{40\mu\text{m}}^{1280\mu\text{m}} D_{p,mm}^3 n(D_{p,mm}) U_\infty(D_{p,mm}) dD_{p,mm}, \quad (5)$$

225 in order to match the unit conversion, the $D_{p,mm}$ is diameter in unit of mm, $n(D_{p,mm})$ is drizzle number
226 concentration in every size bin with a unit of $\# \text{ m}^3 \text{ mm}^{-1}$, and $U_\infty(D_{p,mm})$ is terminal velocity in given
227 size bin, which is calculated from the full Reynolds number theory as in Pruppacher and Klett (2010).

228 The combined threshold of $N_c > 5 \text{ cm}^{-3}$ and $LWC_c > 0.01 \text{ g m}^{-3}$ is used for determining the valid
229 cloud samples and cloud boundaries (Wood, 2005; Zheng et al., 2022b). The complete cloud vertical
230 profiles from sub-cloud to the above-cloud are selected during the ACE-ENA and SOCRATES IOPs, in
231 which the flight strategy includes sawtooth and spiral cloud transects and ramping cloud sampling. The
232 precipitation conditions are determined by whether samples of $N_d > 0.001 \text{ cm}^{-3}$ exists below the cloud
233 base height. In total, the selected numbers of cloud (precipitating cloud) profiles are 18 (13), 26 (13), and
234 28 (24) for ACE-ENA summer and winter IOPs along with SOCRATES, respectively. The detailed
235 selected cloud profiles, with their cloud base heights (z_t), cloud top heights (z_b) and cloud thicknesses
236 ($H_c = z_t - z_b$) are listed in Table S1, along with the cloud profile microphysics.

237 Furthermore, the assessments of ACI are significantly impacted by the MBL dynamic and
238 thermodynamic conditions. Jones et al. (2011) suggested that the MBL would be in a well-mixed and
239 coupled condition when the difference in liquid water potential temperature (θ_L) and total water mixing
240 ratio (q_t) between the bottom of MBL and the inversion layer are less than 0.5 K and 0.5 g/kg,
241 respectively. The cases selected for this study feature both coupled and decoupled MBL conditions,
242 particularly during ACE-ENA summer, which is characterized by anomalously low MBL heights and
243 substantial MBL decoupling. Previous studies found that, under the decoupled conditions, the aerosols,
244 CCN, and moisture sources near the surface are disconnected from the cloud layer aloft, hence exerting
245 much less effective impact on the cloud microphysics (Zheng et al., 2022a; Christensen et al., 2023; Su
246 et al., 2024). Therefore, we adapt and modify the metric in Jones et al. (2011) to calculate the sub-cloud
247 coupled layer, in order to quantify the degree to which aerosols and CCN measured sub-cloud are in a
248 well-mixed state and can represent the actual interaction (or contact) with the cloud layer. In this study,

- Deleted: In
- Deleted: regard, since the
- Deleted: coexist in the selected cloud cases in this study
- Deleted: in
- Deleted: BL
- Deleted: BL
- Deleted: decoupling condition

- Deleted: ensure

257 the q_t and θ_L at the cloud base are calculated, and then their vertical variations are examined starting
258 from the altitude of cloud base (z_b) and looking downward. As such, the coupled point height (z_{cp}) is
259 defined as the altitude where the downward vertical changes in q_t and θ_L exceed 0.5 K and 0.5 g/kg,
260 respectively. Hence, the coupled layer thickness ($H_{cp} = z_t - z_{cp}$) is defined as the layer between the
261 cloud top height (z_t) and coupled point height (z_{cp}), hence the selection of the aerosols and CCN within
262 the below-cloud part of the coupled layer can be viewed as in contact with the cloud. An example of the
263 coupled layer identification is shown in Figure S2. Therefore, the degree of MBL decoupling (D_{cp}) can
264 be quantified as the ratio of the coupled point height (z_{cp}) to the cloud base height (z_b), where $D_{cp} =$
265 z_{cp}/z_b . As shown in Table S1, the ACE-ENA summer feature with highest degree of decoupling
266 (averaged $D_{cp} \equiv 0.504$), compared to the ACE-ENA winter ($D_{cp} \equiv 0.370$) and SOCRATES ($D_{cp} \equiv 0.277$).

267

268 2.2 Aerosol properties

269 The total aerosol number concentrations (N_a) from ACE-ENA and SOCRATES are measured by
270 the airborne Condensation Particle Counter (CPC) models 3772 and 3760A, which counts the number of
271 aerosols with diameter (D_p) larger than 3 nm and 11 nm, respectively (Kuang and Mei, 2019;
272 SOCRATES Low Rate Data, 2022). Additionally, the Passive Cavity Aerosol Spectrometer (PCASP)
273 onboard the ACE-ENA aircraft is capable of sizing the aerosol with D_p ranging from 0.1 μm to 3.2 μm
274 (Goldberger, 2020). While the ultra-high sensitivity aerosol spectrometer (UHSAS) measures the size-
275 resolved aerosol distribution from 0.06 μm to 1.0 μm during SOCRATES (Uin, 2016). Therefore, the
276 number concentrations of accumulation mode aerosols (N_{ACC} , 0.1 μm -1 μm) can be discerned from the
277 PCASP and UHSAS aerosol size distributions. The Aitken mode aerosols (N_{Ait} , $< 0.1 \mu\text{m}$) from the
278 ACE-ENA is given by the fast integrated mobility spectrometer (FIMS), which can size the aerosol down
279 to 9 nm (Olfert et al., 2008), while the N_{Ait} from SOCRATES is limited to 0.06 μm – 0.1 μm due to the
280 limitation of UHSAS. As for the CCN measurements, the ACE-ENA utilized the Dual-Column CCN

Deleted: altitude

Deleted: altitude

Deleted: altitude

Deleted: sub-cloud MBL thickness

Deleted: sub-

Deleted: MBL thickness

287 Counter at two constant supersaturation levels of 0.15% and 0.35% (Uin and Mei, 2019), while the CCN
288 number concentration (N_{CCN}) during SOCRATES was measured under various supersaturation levels
289 from 0.06% to 0.87% using a scanning CCN counter (Roberts and Nenes, 2005). In this study, N_{CCN} at
290 0.35% supersaturation ($N_{CCN0.35\%}$) is used to ensure a direct comparison between ACE-ENA and
291 SOCRATES. The aerosol measurements are in the temporal resolution of 1Hz. Note that the aerosol and
292 CCN data are quality-controlled by removing the data point where the $N_c + N_d$ greater than 5 cm^{-3} or N_d
293 greater than 0.01 cm^{-3} , to filter out the contamination of the cloud droplets, and drizzle water splashing.

294 The sub-cloud aerosols and CCN are selected within the below cloud base part of the coupled
295 layer, which is described in [the](#) last section, in order to better assess the aerosol-cloud interactions. The
296 above-cloud aerosols and CCN are selected between the cloud top and 200 m above. Note that the
297 selection criteria of 200 m above the cloud top would inevitably induce uncertainty in the cloud top ACI
298 assessment, depending on the vertical trend of the individual aerosol profile. Over the Southeast Atlantic,
299 Gupta et al. (2021) conducted an analysis focusing particularly on the differing impacts when biomass
300 burning aerosols are in contact with marine stratocumulus cloud tops, using 100 m above as the
301 demarcation, versus when they are separated by various distances, and found that significant differences
302 were observed in cloud microphysics, owing to different droplet evaporation and nucleation, compared
303 to separated profiles. That result is in agreement with the modeling sensitivity study over the Eastern
304 North Atlantic by Wang et al. (2020), who found that aerosol plumes can exert impacts on the cloud-top
305 microphysics only when they are in close contact with the cloud layer. In most cases, the ACE-ENA
306 feature is a rather stable or slightly decreasing profile within a [few](#) hundred meters above the cloud top,
307 while the long-range transports, particularly during summertime, will induce an elevated aerosol layer in
308 higher altitudes that is not in contact with the cloud layer. [The](#) frequent new particle formation events
309 during SOCRATES will significantly alter the free-troposphere Aitken mode aerosol budget, they would
310 need to further subside [to impact the cloud](#) (McCoy et al., 2021; Zhang et al., 2023). Therefore, the 200

Deleted: couple

Deleted: While the

Deleted: down

314 m criteria used in this study captures the close-to-cloud aerosol plumes and provides enough sample
315 size for statistical analysis.

Deleted: criteria
Deleted: are in the reconciliation of getting

316 **3. Aerosol, cloud, and drizzle properties of selected cases**
317

Deleted: ¶

318 **3.1 Aerosols and CCN in above- and sub-cloud regimes**

319 The probability density functions (PDFs) of aerosols, CCN, and cloud microphysical properties
320 from selected cases during the ACE-ENA and SOCRATES field campaigns are presented in Figure 1.
321 Notably, the N_a , N_{Acc} and $N_{CCN0.35\%}$ values from the SOCRATES are the highest among the three IOPs,
322 followed by the ACE-ENA summer and winter as illustrated in both above-cloud (Figs. 1a-1c) and sub-
323 cloud regimes (Figs. 1d-1f). Such variations can be linked to the different aerosol sources in the ACE-
324 ENA and SOCRATES regions, especially during the summer and winter seasons over the Azores.

Deleted: disparate

325 In the SOCRATES region, according to the previous studies involving back-trajectory analyses,
326 dominant air masses within the MBL primarily originate from the south or from the west, skirting the
327 Antarctic coast (Zhang et al., 2023), while the air masses above the MBL follow a similar transport
328 pathway, they can also originate from the tip of southern Africa and be transported southeast along the
329 warm conveyor belt (McCoy et al., 2021). The SOCRATES above-cloud aerosols (674.6 cm^{-3}) are
330 primarily constituted by the Aitken mode aerosols because the mean N_{Acc} is only 62.5 cm^{-3} . Previously,
331 McCoy et al. (2021) reported average values of 680.69 cm^{-3} , 546.28 cm^{-3} and 465.05 cm^{-3} for mid-
332 troposphere, above and below cloud for the multiple SOCRATES cases, respectively. For individual
333 cases, the above cloud aerosols vary from a couple hundred to over a thousand particles per cubic
334 centimeter (McCoy et al., 2021; Zhang et al., 2023). These aerosols are predominantly produced from
335 the oxidation of biogenic gases, notably the dimethyl sulfide (DMS) emitted by marine biological
336 productivity (Sanchez et al., 2018; McCoy et al., 2020). The rising air currents in MBL transport these
337 particles into the free troposphere (FT) with dominant aerosol population over the SO (McCoy et al.,
338 2021; Sanchez et al., 2021). Hence, it reinforces the notion that the SO represents a pre-industrial marine

Deleted: transport

Deleted: cm-3,

Deleted: While for the

Deleted: a

Deleted: And hence

348 environment where the influence of anthropogenic and biomass-burning aerosols is mostly negligible
349 (McCoy et al., 2020, 2021).

350 Conversely, the ENA region experiences aerosols of varied origins, spanning maritime air masses
351 to those heavily influenced by continental emissions from North America or Northern Europe, especially
352 during the summertime (Logan et al., 2014; Wang et al., 2020). The summertime air mass back-
353 trajectories within the MBL strongly feature recirculating flow around the Azores high. During the
354 wintertime, however, the air masses predominantly originate in the FT, are transported above the MBL,
355 and are then further entrained down to the MBL by large-scale subsidence, indicating less influence from
356 continental pollution (Y. Wang et al., 2021b). During the summer ACE-ENA campaign, the MBL is
357 enriched by sulfate and carbonaceous particles (Y. Wang et al., 2021b; Zawadowicz et al., 2021). This
358 enhancement is attributed both to local generation from DMS and to the long-range transport from the
359 continental air masses, resulting in the mean N_a of 312.6 cm^{-3} and 301.5 cm^{-3} for above- and sub-cloud
360 regimes, respectively. The ACE-ENA winter exhibits the lowest aerosol and CCN concentrations,
361 predominantly sourced from local maritime influences, and coupled with reduced continental air mass
362 intrusions (Zheng et al., 2018; Y. Wang et al., 2021b).

363 Figure 1a reveals that there are more above-cloud N_a during the three IOPs than sub-cloud values,
364 especially during the SOCRATES. The higher above-cloud N_a values from the three IOPs are primarily
365 contributed by Aitken mode aerosols because their corresponding N_{Acc} values are much lower (Figs.
366 1a&b). It is interesting to note that the above-cloud $N_{CCN0.35\%}$ values exceed the N_{Acc} for all three IOPs
367 (Figs. 1b&c), implying that a significant fraction of Aitken mode aerosols can be activated to become
368 CCN, corroborating findings from earlier studies (McCoy et al., 2021; Zheng et al., 2021). For the sub-
369 cloud regime, the N_a values during SOCRATES and ACE-ENA winter are ~70-80% of their
370 corresponding above-cloud values, and the N_a during ACE-ENA summer is almost identical to its above-
371 cloud value. Notice that the sub-cloud N_{Acc} values from three IOPs are more than double the above-cloud

Deleted: of

373 N_{Acc} values, and most of the sub-cloud accumulation mode aerosol can be activated to become CCN at
374 SS of 0.35%. It is interesting to note that the higher $N_{CCN0.35\%}$ at sub-cloud layer during SOCRATES
375 may partially result from the cloud process on aerosols (Figs. 1e&f), which is suggested by previous
376 studies (McCoy et al., 2021; Zhang et al., 2023) and will be further discussed in Section 3.1.

377 To further investigate the above- and sub-cloud aerosol properties from three IOPs, the aerosol
378 droplet size distributions are analyzed in Figure 2. It is evident that SOCRATES aerosols have the highest
379 concentrations of Aitken mode particles ($D_p = 0.06 - 0.1 \mu\text{m}$, given that the $< 0.06 \mu\text{m}$ is not available
380 from UHSAS) for both the above- and sub-cloud regimes. McCoy et al. (2021) and Zheng et al. (2021)
381 identified analogous origins and formations of the above-cloud Aitken mode aerosols over both the SO
382 and ENA regions and concluded that these aerosols primarily originate from the nucleation of photo-
383 oxidation products of DMS, notably H_2SO_4 and MSA, in the free troposphere (FT). The differential
384 concentrations can be ascribed to the fact that sea-surface DMS concentrations in the SO are generally
385 higher than those in the ENA region (Aumont et al., 2002; Zhang et al., 2023). Moreover, DMS emissions
386 in the ENA during summer surpass those during winter (Zawadowicz et al., 2021). For the accumulation
387 mode aerosols ($0.1 - 1 \mu\text{m}$), the N_{Acc} values for both above- and sub-cloud regimes during SOCRATES
388 decrease monotonically with particle size. The results in Figure 2 further support the finding that Aitken
389 mode aerosols are dominant over the SO. The N_{Acc} values during ACE-ENA show slight uplifts for the
390 small accumulation mode aerosols ($< 0.3 \mu\text{m}$), particularly for summer, reflecting the signal of potential
391 long-range transport of fine-mode aerosols (Wang et al., 2020; Y. Wang et al., 2021b). Consequently,
392 such comparison reinforces the notion that the SO represents a largely pre-industrial marine environment,
393 wherein the influence of anthropogenic and biomass-burning aerosols is minimal (McCoy et al., 2020,
394 2021; Zhang et al., 2023).

395 When contrasting the aerosol size distributions in the sub-cloud regime (Fig. 2b) with those in the
396 above-cloud regime, the influence of cloud processing on aerosols is discernibly non-trivial, particularly

Deleted:),

398 under the cloud-topped MBL conditions examined in this study. ~~The FT aerosols can be entrained down~~
399 and contribute to the population of Aitken mode aerosols within the MBL, ~~and~~ the sub-cloud aerosols
400 can also be subject to the influence of new particle formation in the upper MBL, though arguably less
401 effective than those within the FT (Zheng et al., 2021). Additionally, in-cloud Brownian capture can lead
402 to a substantial reduction in Aitken mode aerosols (Hudson et al., 2015; Wyant et al., 2022), providing
403 the rationale for the observed decrease in Aitken mode aerosols ~~from above- to~~ the sub-cloud regime,
404 especially for particles smaller than 0.07 μm . In addition, cloud chemical processing, such as the
405 aqueous-phase condensation of sulfuric gas onto the aerosol cores inside the cloud droplets, is
406 particularly pronounced during the transitioning of Aitken mode aerosols to accumulation mode aerosols
407 (Hudson et al., 2015; Zhang et al., 2023).

408 From both above- to sub-cloud regimes, the larger Aitken mode aerosols ($> 0.07 \mu\text{m}$) can be
409 effectively enlarged to accumulation mode aerosols through coagulation and water vapor diffusional
410 growth (Covert et al., 1996), contributing to the elevated accumulation mode aerosol distribution and
411 increased N_{Acc} in the sub-cloud regime. These processes are ~~evidenced by the decrease of critical~~
412 supersaturations from above-cloud (between 0.35% - 0.4%) to sub-cloud (between 0.3% - 0.35%) during
413 SOCRATES (Fig. S3) because the aerosol droplet sizes are enlarged and more readily become CCN.
414 Furthermore, the collision-coalescence combines mixtures of large and small cloud droplets, and results
415 in the sub-cloud aerosol residuals shifting towards the larger size, ~~upon the drizzle droplet evaporation~~
416 below the cloud. This partially elucidates the observed increase in the tail-end of the accumulation mode
417 aerosol distribution for all three IOPs. The elevation in sub-cloud coarse mode aerosols observed for both
418 ACE-ENA IOPs (as seen in Fig. 2) can be attributed ~~to the evaporation of collision-coalescence-enlarged~~
419 ~~drizzles~~ and the intrusion of sea spray aerosols (e.g., sea salt), ~~as~~ illustrated and analyzed based on a
420 ~~summertime~~ case study ~~that~~ exhibits the signal of cloud-processing aerosols (Zheng et al., 2022b), ~~and~~
421 the long-term aerosol physicochemical properties over the ARM-ENA ground-based observatory (Zheng
422 et al., 2018), ~~particularly~~ during the winter season where the production of sea spray aerosol is prevalent.

Deleted: While the

Deleted: further

Deleted: in

Deleted: particularly

Deleted: ,

Deleted: (often manifested as drizzle).

Deleted: both

Deleted: enlargement process

Deleted:). As

Deleted: during summertime

Deleted: as well as

Deleted:),

435

436 3.2 Bulk cloud microphysical properties distribution

437 The PDFs of MBL cloud microphysical properties (N_c , r_c , LWC_c) derived from aircraft in-situ
438 measurements from the three IOPs are shown in Figures 1g-1i. The mean microphysical properties for
439 the individual cloud profiles are listed in Table S2. The results in Figure 1 have demonstrated that
440 aerosol/CCN sources and concentrations, especially from the sub-cloud regime, play an important role
441 in cloud droplet formation and evolution. For example, the SOCRATES has the highest sub-cloud
442 aerosols and CCN, and subsequently feature a larger number of smaller cloud droplets, given the highest
443 N_c (148.3 cm^{-3}) and smallest r_c ($8 \text{ }\mu\text{m}$) among the three IOPs. These results have further confirmed and
444 reassured our understanding of the aerosol first indirect effect: more aerosols induce more and smaller
445 cloud droplets (higher N_c and smaller r_c) under constrained liquid water content conditions, thus the
446 MBL clouds reflect more incoming solar radiation (Twomey, 1977). The ACE-ENA wintertime clouds
447 feature the fewest N_c (70.6 cm^{-3}) and largest r_c ($9.8 \text{ }\mu\text{m}$), while the N_c and r_c (89.4 cm^{-3} and $9 \text{ }\mu\text{m}$) during
448 ACE-ENA summer fall between the SOCRATES and ACE-ENA winter values. Considering the aerosol
449 competing effect against the available water vapor, the relatively abundant aerosols in SOCRATES might
450 account for the narrower r_c distribution, which peaks between $6 - 10 \text{ }\mu\text{m}$. SOCRATES has a lower cloud-
451 layer water vapor mixing ratio (figure not shown) compared to ACE-ENA because the SO region has
452 been observed to contain less precipitable water vapor than the ENA region due to the colder sea surface
453 temperatures (Marcovecchio et al., 2023). Therefore, the aerosol and cloud properties in Figure 1 promise
454 further examination of different cloud microphysical responses to aerosols via the ACI process. Note that
455 the $N_{CCN0.35\%}$ and N_c values are lower than N_c values during the ACE-ENA winter IOP, which is also
456 confirmed in previous studies (J. Wang et al., 2022; Wang et al., 2023). This interesting phenomenon
457 can potentially be attributed to a combination of factors, including lower MBL aerosol sources, stronger
458 in-cloud coalescence-scavenging depletion of sub-cloud aerosols, and the aircraft snapshots capturing

Deleted: Wang et al., 2022; Wang et al., 2023), which is also confirmed in previous studies (J.

461 the equilibrium states of aerosols and cloud due to enhanced aerosol activations induced by stronger
462 updrafts during the ACE-ENA winter (J. Wang et al., 2022). This thereby compels further investigation
463 into the potential impacts of precipitation on the MBL CCN budget. These aerosol-cloud-precipitation
464 interactions (ACPIs) will be discussed in Section 4.

465

466 3.3 Vertical distributions of cloud and drizzle microphysics

467 The vertical distributions of the cloud and drizzle microphysical properties within the cloud layer
468 from the three IOPs are shown in Figure 3. To ensure the representativeness of the vertical profiles, all
469 the in-cloud samples are vertically smoothed using a triangular moving average method, and are inverse
470 distance weighted in every 50 m moving altitude windows. Furthermore, the altitude is then normalized
471 by $z_i = \frac{Z - Z_{base}}{Z_{top} - Z_{base}}$, where $z_i = 0$ denotes cloud base and $z_i = 1$ denotes cloud top. Consistent with
472 previous discussions on the bulk microphysics distribution, the mean N_c values from SOCRATES are
473 consistently higher than ACE-ENA summer and winter for the entire cloud layer, with a slight increase
474 ranging from the cloud base to the upper-middle part ($z_i \approx 0.85$) and then decreasing toward the cloud
475 top due to cloud-top entrainment (Fig. 3a). All r_c values from the three IOPs show a near-linear increase
476 from cloud base to top, with the smallest values observed during SOCRATES and the largest values
477 observed during ACE-ENA winter (Fig. 3b).

478 The warmer and drier air near the cloud top entrains into the cloud layer and further mixes
479 downward, often resulting in the evaporation of small cloud droplets and the shrinking of droplet sizes,
480 which oppose condensational growth (Desai et al., 2021). Decreases in both N_c and LWC_c , and the
481 reduced growth of r_c near the cloud top ($z_i > 0.85$) support signals of cloud-top entrainment mixing
482 during all three IOPs. It is interesting to note that the r_c values from SOCRATES increase monotonically
483 from cloud base to top, while the r_c values from both ACE-ENA summer and winter increase until $z_i \approx$
484 0.8 and then remain nearly constant, although all of their N_c values (at $z_i \approx 0.8$) decrease towards the

Deleted: by

486 cloud top. When dry air entrainment occurs at the cloud top, some of the upper-level smaller cloud
487 droplets will evaporate, which leads to decreases in N_c (Fig. 3a). As cloud-top entrainment mixing can
488 shrink large cloud droplets via evaporation, depending on the entrainment mixing rate, the nearly
489 constant r_c values (at $z_i > 0.8$) might represent the equilibrium balance between two competing
490 processes: cloud droplet condensational and collision-coalescence growths, and the entrainment mixing
491 evaporation effects.

492 While carrying the distinct discrepancies in the mean values for all layers, the N_c and r_c from
493 ACE-ENA summer and winter clouds experienced similar vertical evolutions as the SOCRATES. The
494 increases of r_c (Δr_c) from cloud base to cloud top are $4.03 \mu\text{m}$, $4.78 \mu\text{m}$ and $5.85 \mu\text{m}$, with percentage
495 increases of 66%, 68% and 79%, for SOCRATES, ACE-ENA summer and winter, respectively. Even
496 though, theoretically, the condensational growth effect would be more pronounced on smaller cloud
497 droplets due to their smaller surface area (Wallace and Hobbs, 2006), SOCRATES exhibits the thickest
498 mean cloud thickness but experienced the least r_c increase among the three IOPs. This suggests that high
499 aerosol loadings are limiting the overall growth of the cloud DSD in SOCRATES clouds, while the ACE-
500 ENA winter clouds show the strongest r_c increase, in contrast. This comparison indicates different cloud
501 microphysical responses to aerosol perturbations in the three IOPs, which will be further discussed in
502 Section 4.1. The LWC_c values from the three IOPs are comparable to each other. The vertical
503 distributions of MBL cloud microphysical properties examined in this study are in good agreement with
504 the previous studies conducted on these two field campaigns (Wu et al., 2020a; Y. Wang et al., 2021a; J.
505 Wang et al., 2021; Wang et al., 2023). In addition, the cloud adiabaticity is defined as $f_{ad} =$
506 LWC_c/LWC_{ad} , where the LWC_{ad} denotes adiabatic LWC (Wu et al., 2020b). As shown in Figure S4,
507 the clouds from all three IOPs feature certain levels of sub-adiabaticity above the cloud base. Considering
508 the inter-cloud layer-mean f_{ad} , the campaign-mean f_{ad} values are 0.689 ± 0.229 , 0.542 ± 0.143 , and
509 0.490 ± 0.207 for SOCRATES, ACE-ENA summer and winter, respectively. It is well known that cloud

Deleted: increases

Deleted: suggests

Deleted: has been

513 sub-adiabaticity is primarily induced by the in-cloud collision-coalescence and the entrainment mixing
514 processes (Hill et al., 2009; Braun et al., 2018; Gao et al., 2020; Wu et al., 2020b).

515 To quantitatively evaluate the impact of cloud-top entrainment mixing rate on cloud droplets, we
516 adapt the method of Albrecht et al. (2016), where the cloud-top entrainment rate (w_e) can be expressed
517 as

$$518 \quad w_e = A_\sigma * \sigma_w / R_{i\sigma}, \quad (6)$$

519 where the turbulence kinetic energy (TKE) dissipation coefficient A_σ is empirically taken as 26 as in
520 Albrecht et al. (2016), and the $R_{i\sigma}$ is the buoyancy Richardson number calculated by $(g/\theta_0) *$
521 $(\Delta\theta_v h / \sigma_w^2)$. σ_w denotes the standard deviation of vertical velocities taken near the cloud top ($z_i > 0.9$),
522 and h is the MBL height. θ_0 is the reference potential temperature and $\Delta\theta_v$ is the virtual potential
523 temperature difference across the temperature inversion layer above the cloud. Given the valid cloud top
524 virtual potential temperature and vertical velocity measurements for the selected cloud cases, the
525 averaged w_e values are $0.570 \pm 0.834 \text{ cm s}^{-1}$, $0.581 \pm 0.560 \text{ cm s}^{-1}$, and $0.960 \pm 1.127 \text{ cm s}^{-1}$ for SOCRATES,
526 ACE-ENA summer and winter, respectively. The stronger w_e during ACE-ENA winter might be induced
527 by the generally weaker cloud-top inversions and stronger near-cloud top turbulence, compared to the
528 summertime when the ENA is dominated by the large-scale high-pressure system (Ghate et al., 2021).
529 Considering the near cloud-top proportion of cloud where the LWC_c experienced decrease, the difference
530 in LWC_c (between the cloud top value and the upper-middle cloud maximum for the mean profiles) for
531 the ACE-ENA summer (-0.032 g m^{-3}) is higher than the reductions in winter (-0.018 g m^{-3}) and
532 SOCRATES (-0.009 g m^{-3}), albeit that the w_e for ACE-ENA summer is comparable to SOCRATES, and
533 much lower than ACE-ENA winter values. Within the above-cloud inversion layer, the temperature
534 (water vapor mixing ratio) differences ΔT (Δq) are 1.76 K (-1.75 g kg^{-1}), 1.54 K (-1.66 g kg^{-1}) and 1.48
535 K (-1.09 g kg^{-1}) for SOCRATES, ACE-ENA summer and winter, respectively. Therefore, the warmer
536 and dryer entrained air can partially contribute to the greater LWC_c reduction and the lower f_{ad} (0.39)

537 during the ACE-ENA summer than those during the ACE-ENA winter ($f_{ad} = 0.45$) and SOCRATES
 538 ($f_{ad} = 0.66$) near the cloud top (Fig. S4). For the three IOPs, the N_c and LWC_c exhibited stable trends
 539 from the cloud base, followed by noticeable decreases near the cloud top mixing zone, while the changes
 540 in r_c trends near the cloud top were not as dramatic as the others. Such characteristics of the cloud
 541 microphysics vertical profiles indicate the signal of inhomogeneous mixing, which occurs when dry and
 542 warm air mixes unevenly and slowly with the cloud air, hence partially evaporating the cloud droplets
 543 (Lehmann et al., 2009; Lu et al., 2011). The results are consistent with findings in stratocumulus clouds
 544 over multiple field campaigns (Brenguier et al., 2011; Jia et al., 2019) and with the findings for selected
 545 cases during the ACE-ENA (Yeom et al., 2021) and the SOCRATES (Sanchez et al., 2020). The near-
 546 cloud top r_c profiles ($z_i > 0.8$) for the ACE-ENA cases exhibit fewer increases compared to the
 547 SOCRATES, which could be possibly attributed to more effective mixing due to the stronger entrainment
 548 rate, particularly during the ACE-ENA winter, eventually reaching a smaller equilibrium in terms of
 549 mean sizes.

550 Figures 3d-3f illustrate the normalized profiles of MBL drizzle microphysical properties. The N_d
 551 values from the three IOPs mimic each other, which all maximize at the cloud top and then monotonically
 552 decrease toward the cloud base (Fig. 3d), while their LWC_d values follow a similar trend, albeit with
 553 relatively large differences (Fig. 3f). In contrast to the N_d and LWC_d trends, the D_{mmd} gradually increase
 554 from cloud top to cloud base (Fig. 3e), making physical sense since the drizzle droplets are typically
 555 formed near cloud top and continuously grow via collision-coalescence process while falling. The ACE-
 556 ENA wintertime drizzle D_{mmd} and LWC_d are distinctively larger than those in summertime and
 557 SOCRATES. It is interesting to note that near the cloud top ($z_i > 0.9$), the ACE-ENA winter has
 558 comparable N_d but much larger D_{mmd} than the other two IOPs, suggesting that there were more large
 559 drizzle embryos formed from large cloud droplets (Fig. 3b) during ACE-ENA winter. It is noteworthy
 560 that the D_{mmd} in the lower-half region of the ACE-ENA winter clouds experienced rapid growth from

Deleted: a

Deleted: trend

Deleted: a

Deleted: decrease

Deleted: trend

Deleted: not rapidly

Deleted:),

Deleted: While the

Deleted: more constant variation

Deleted:

571 ~80 μm to ~105 μm (Fig. 3e), and this increment of ~25 μm contributed to most of the D_{mod} growth
572 from cloud top to cloud base (33.5 μm), indicating a stronger warm-rain process during the winter.

573 In order to further analyze the cloud-to-drizzle conversion processes, the cloud and drizzle droplet
574 size distributions (DSD) are categorized into four segments based on their relative position within the
575 cloud layer (Fig. 4): upper cloud ($z_i > 0.8$, Fig. 4a), upper-middle cloud ($0.5 \leq z_i < 0.8$, Fig. 4b), lower-
576 middle cloud ($0.2 \leq z_i < 0.5$, Fig. 4c) and lower cloud ($z_i < 0.2$, Fig. 4d). The cloud DSDs ($D_p < 40$
577 μm) from the three IOPs gradually shift towards larger sizes, moving from the lower to the upper cloud
578 regions. This is accompanied by the narrowing of the cloud DSD ranges, as evidenced by the decline in
579 the relative dispersion of cloud droplets (ϵ), which is defined as the ratio between the standard deviation
580 and the mean radius of the distribution. At the lower portion of the cloud (Fig. 4d), the relatively greater
581 value of ϵ represents the co-existence of the newly formed small cloud droplets from recently activated
582 CCNs and the sedimentation of larger droplets from the upper sections of the cloud. In addition, the
583 discrepancies in ϵ between the three IOPs may be attributed to the sub-cloud aerosol differences, which
584 essentially resided in different microphysical regimes. Y. Wang et al. (2021a) stated that higher aerosol
585 loading would lead to increased ϵ due to the water vapor competition effect, supporting the discrepancy
586 between SOCRATES and ACE-ENA summer IOPs, which can be categorized as a water-vapor-limited
587 regime. Meanwhile, the ACE-ENA wintertime IOP exhibits characteristics of an aerosol-limited regime,
588 in which the cloud DSDs tend to be narrower than in the water-limited regime, due to enhanced droplet
589 growth, and the ϵ values further decrease with height via the condensational narrowing effect (J. Chen et
590 al., 2018).

591 Notably, the cloud DSDs during ACE-ENA winter exhibit a more pronounced negative skew (to
592 the left) than those during ACE-ENA summer, which can be partially attributed to the activation of more
593 sub-cloud coarse mode aerosols becoming larger cloud embryos, as demonstrated in Fig. 2. These coarse
594 mode aerosols, whether from primary production of sea spray or the residuals of evaporated drizzle drops,

Deleted: cloud relative dispersion (ϵ). The

Deleted:) is a parameter that represents the DSD and

Deleted: clearly

Deleted: attribute

Deleted: to become

Deleted: from

601 are more easily activated (or re-activated) into larger cloud droplets when they intrude (or recirculate)
602 into the cloud layer (Hudson and Noble, 2020; Hoffmann and Feingold, 2023). Nevertheless, it is
603 challenging to pinpoint the actual origins of coarse mode aerosols from the perspective of aircraft
604 observational snapshots, thus requiring further numerical modeling work. For the four cloud portions
605 from cloud base to cloud top, the skewness of summertime (wintertime) cloud DSDs are 0.627 (0.271),
606 0.358 (0.175), 0.098 (-0.063), and -0.362 (-0.554), respectively. Ascending within the cloud, the process
607 of water vapor condensation perpetually pushes the DSD towards larger sizes, culminating in a more
608 negatively skewed DSD. Concurrently, the cloud-top entrainment mixing plays a pivotal role in
609 minimizing ε in the upper cloud region, as elaborated by Lu et al. (2023). Note that in the upper region
610 of the cloud (Fig. 4a), the ACE-ENA winter clouds contain more cloud droplets close to 40 μm , albeit
611 the mean N_c is lower. This scenario is conducive to the formation of larger drizzle embryos compared to
612 summertime clouds, as depicted in Fig. 3e. In comparison, the SOCRATES clouds feature a pronounced
613 log-normal DSD than the ACE-ENA, as the DSDs peak at $D_p \sim 15 \mu\text{m}$ throughout the cloud, and
614 subsequently, the lack of larger cloud droplets resulted in the smaller drizzle embryos near the cloud top.
615 As the newly formed drizzle drops descend and continuously grow through the collision-coalescence
616 process, the drizzle DSDs ($D_p > 40 \mu\text{m}$) are noticeably broadened. From upper to lower cloud regions,
617 the longer tails of the drizzle DSDs expand at the cost of smaller drizzle drops and cloud droplets via the
618 collision-coalescence process. The clouds observed during ACE-ENA, especially in wintertime, contain
619 more large drizzle drops ($D_p > 200 \mu\text{m}$) than SOCRATES, which is reflected in the distinct differences
620 in the vertical D_{mod} as shown in Fig. 3e.

621 It has been intensively studied that in-cloud turbulence can stimulate collision-coalescence and
622 consequently enhance the drizzle evolution processes (Pinsky et al., 2007; Grabowski and Wang, 2013;
623 Wu et al., 2017; S. Chen et al., 2018). The turbulence strength is characterized by the turbulence kinetic
624 energy (TKE), which is calculated as:

625 $TKE = \frac{1}{2} (\overline{u'^2} + \overline{v'^2} + \overline{w'^2})$, (7)

626 where the turbulent perturbations of vertical ($\overline{w'^2}$) and horizontal ($\overline{u'^2}$ and $\overline{v'^2}$) components are
627 calculated as the simple moving variance in a 10s window centered at the measurement time, without
628 window weighting function, using 1Hz data for all three IOPs. The w data is confined to an absolute
629 aircraft roll angle of less than 5° (Cooper et al., 2016). Given the average aircraft ground speed of ~140
630 m/s and vertical speed of ~5 m/s (Atlas et al., 2020), the smallest resolved wavelength is 140 m. Hence,
631 within the 10s moving window, the ~50 m in the integral vertical range is able to resolve the eddies up
632 to ~1400 m in size, and preserve the potential of capturing the inertial subrange.

Deleted: Atlas

633 As shown in Figure 5, the vertical wind variances (Fig. 5b) in ACE-ENA winter (layer-mean of
634 $0.244 \text{ m}^2 \text{ s}^{-2}$) are generally higher than those in summer ($0.153 \text{ m}^2 \text{ s}^{-2}$) and SOCRATES ($0.147 \text{ m}^2 \text{ s}^{-2}$),
635 while the horizontal wind variances (Fig. 5c & d) are comparable between ACE-ENA winter and summer
636 but much higher than the SOCRATES, resulting in higher TKE during ACE-ENA. Note that the higher
637 w'^2 near cloud top corresponds to the stronger entrainment rate in wintertime ACE-ENA. Near the cloud
638 top, turbulence effectively enhances coalescence between the larger cloud droplets, primarily by
639 increasing the relative velocities between droplets (Magaritz-Ronen et al., 2016; Ghate and Cadettu,
640 2019), and this is especially true for the vertical component w'^2 of TKE. While the horizontal turbulence
641 components, the u'^2 and v'^2 can also play a role in mixing the ambient air masses and contribute to the
642 broadening of DSD (Wu et al., 2017). The use of TKE provides an illustration that in-cloud turbulence
643 during ACE-ENA might be slightly stronger than that observed during SOCRATES. That being said, the
644 quantitative evaluation of the turbulent enhancement of collision-coalescence requires access to the eddy
645 dissipation rate, as typically used in model parameterizations (Grabowski and Wang, 2013; Witte et al.,
646 2019). The smallest scales resolvable with the 1Hz measurement used in this study are on the order of
647 140 meters, thus capturing only the larger-scale end of the inertial subrange and larger turbulent motions.
648 Consequently, the ability to resolve smaller eddies and turbulent structures, crucial for understanding the

Deleted: Witte

651 energy cascade within the inertial subrange, is limited by the too-coarse spatial and temporal resolutions
652 and aliasing issues (Siebert et al., 2010; Muñoz-Esparza et al., 2018; Kim et al., 2022). Therefore, to
653 fully resolve the spectrum of turbulence and quantitatively examine energy dissipation and mixing
654 processes, access to higher-frequency measurements is required to capture smaller eddies within the
655 inertial subrange (Siebert et al., 2010; Lu et al., 2011; Waclawczyk et al., 2017). Additionally, further
656 quantifying the entrainment-mixing mechanisms also requires high-frequency eddy dissipation and
657 accurate examination of the mixing time scale (Lehmann et al., 2009; Lu et al., 2011) for individual
658 profiles. Though currently beyond the scope of this study, utilizing the high-rate measurements of
659 velocities available from SOCRATES (at 25Hz) and ACE-ENA (at 20Hz) to explore those mechanisms
660 further will be of interest to future investigations.

Deleted: the

Deleted: quantification of

Deleted: profile

Deleted: for

661 Drizzle formation and evolution in the ACE-ENA winter clouds are noticeably stronger than in
662 the other two IOPs, which could be attributed to multiple factors. First, the ambient aerosols and CCN
663 during winter are substantially fewer, featuring clean environments that promote the formation of
664 generally larger cloud droplets due to the availability of more water content per droplet. Larger cloud
665 droplets are more likely to collide and coalesce into drizzle drops, leading to relatively heavier
666 precipitation (Chen et al., 2011; Duong et al., 2011; Mann et al., 2014). Furthermore, the wintertime
667 clouds feature deeper cloud layers with mean thickness of (392.4 m) compared to the summertime clouds
668 (336.3). In a thicker cloud layer with sufficient turbulence, the residence times of large cloud droplets
669 and drizzle drops are elongated, and the chance of collision-coalescence growth can be effectively
670 increased by recirculating the drizzle drops (Brost et al., 1982; Feingold et al., 1996; Magaritz et al.,
671 2009; Ghate et al., 2021). Additionally, the prevalence of precipitation-evaporation-induced MBL cold
672 pools, which disturb the MBL thermodynamics and contribute to turbulent mixing (Zuidema et al., 2017),
673 during the wintertime might provide strong dynamical forcing to the warm-rain process (Jenson et al.,
674 2021; J. Wang et al., 2022; Smalley et al., 2024). As a result, the ACE-ENA wintertime drizzle DSD is
675 sufficiently broadened, and the D_{mmd} is enlarged toward the cloud base. In comparison, although the

Deleted:).

681 SOCRATES exhibits even thicker clouds (487.4 m), the drizzle processes are seemingly suppressed by
682 the much higher ambient aerosol and CCN concentrations.

683

684 **4 Aerosol-cloud-precipitation interactions (ACPIs)**

685 **4.1 Cloud microphysical responses on aerosols**

686 The impacts of different aerosol loadings on the cloud microphysical properties can be assessed
687 by the aerosol-cloud interaction (ACI) indices, which can be quantified as:

$$688 \quad ACI_N = \frac{\partial \ln(N_c)}{\partial \ln(N_{CCN,0.35\%})}, \quad (8)$$

689 and

$$690 \quad ACI_r = -\frac{\partial \ln(\tau_c)}{\partial \ln(N_{CCN,0.35\%})}, \quad (9)$$

691 which emphasizes the cloud microphysical responses to CCN via the relative logarithmic change of N_c
692 and τ_c to the change in $N_{CCN,0.35\%}$ (Feingold et al., 2003; McComiskey et al., 2009). Physically, the ACI
693 process involves aerosols intruding into the cloud layer, activating as cloud droplets, and subsequently
694 altering cloud DSD and dispersion (Zheng et al., 2022a&b) under various water vapor availabilities.
695 Therefore, the cloud microphysical responses within the lower region of the cloud are assessed, which is
696 the first stage in which the sub-cloud CCN can directly interact with the cloud droplets. Furthermore, the
697 similarity in the vertical integral of LWC_c (as shown in Fig. 3c) provides comparable liquid water
698 between three IOPs for the assessment of newly generated cloud embryos from activated CCN because
699 the ACI_r is normally assessed under a fixed liquid water (Zheng et al., 2020).

700 Considering all the cases from three IOPs with available CCN measurements (some cases without
701 CCN measurements during SOCRATES), the N_c and τ_c at the lower cloud ($z_i < 0.2$) are plotted against
702 the sub-cloud $N_{CCN,0.35\%}$ in Figure 6, and the ACI indices are calculated as $ACI_{N,CB}$ and $ACI_{r,CB}$ (CB
703 denoting the assessment near the cloud base). Note that the availability of valid sub-cloud measurements
704 inevitably limits the sample size, especially for SOCRATES, as shown in Table S2. As shown in Figure

705 6a, the $ACI_{N,CB}$ for the ACE-ENA wintertime (0.748) is higher than the summertime (0.617), indicating
706 that N_c is more sensitive to the sub-cloud $N_{CCN,0.35\%}$ during the winter. In other words, aerosols intruding
707 into the cloud layer are easily activated to become cloud droplets. The N_c sensitivity for the SOCRATES
708 cloud (0.692) lies between the two ACE-ENA IOPs. The $ACI_{N,CB}$ values from three IOPs are generally
709 higher than the ACI_N values from the layer-mean N_c against the sub-cloud $N_{CCN,0.35\%}$ (not shown).
710 Previous studies have shown that the enhanced vertical turbulence (updraft velocity) can effectively
711 facilitate CCN replenishment into the cloud layer (Hu et al., 2021; Zheng et al., 2022a&b) and increase
712 the actual in-cloud supersaturation (Brunke et al., 2022), thus leading to a more efficient cloud droplet
713 formation, enhancing the $ACI_{N,CB}$. By correlating the mean TKE values with the CCN activation ratio
714 ($N_c/N_{CCN,0.35\%}$) for all individual cloud cases, the three IOPs show moderate but statistically significant
715 correlation coefficients of 0.36, 0.55, and 0.51 for ACE-ENA summer, winter, and SOCRATES,
716 respectively. This result reinforces the notion that the CCN activation fractions, particularly during the
717 wintertime ACE-ENA, are significantly correlated with in-cloud turbulence intensities. Furthermore,
718 more coarse mode aerosols during ACE-ENA winter are also favorable to the activation efficiency
719 (Dusek et al., 2006).

720 As for the r_c responses to CCN (Fig. 6b), the typical Twomey effect, where more CCN compete
721 against available water vapor and result in smaller cloud droplets, is evidenced by different cloud
722 susceptibility between the three IOPs. The SOCRATES features a higher $ACI_{r,CB}$ (0.311), suggesting
723 that an increase in $N_{CCN,0.35\%}$ can result in a significant decrease in r_c , compared to ACE-ENA summer
724 (0.206) and winter (0.263). Although the absolute range of variation for r_c during SOCRATES is smaller,
725 the slope is much deeper (Fig. 6b). Recall that the sub-cloud $N_{CCN,0.35\%}$ during SOCRATES is generally
726 higher and is constituted by more small-sized aerosols (as indicated in Fig. 2b). Consequently, after
727 activation, the lower part of the cloud exhibits a higher number of smaller cloud droplets, as shown in
728 Fig. 4d, even under the relatively less $N_{CCN,0.35\%}$ condition for SOCRATES. Therefore, as more CCN

729 intrudes into the cloud, the competition for water vapor among newly-activated cloud droplets becomes
730 more pronounced, given similar water availability. In contrast, the presence of larger cloud droplets near
731 the cloud base, whether activated from coarse-mode aerosols or remaining as residuals from collision-
732 coalescence, would elevate the r_c especially under the relatively more CCN condition, hence inevitably
733 dampening the $ACI_{r, CB}$ during ACE-ENA. However, a more comprehensive investigation into the cloud
734 microphysical responses to CCN intrusions under a larger range of various water supply conditions, and
735 further untangling the ACI from the meteorological influences, will require additional aircraft cases from
736 more field campaigns, for instance the VAMOS Ocean-Cloud-Atmosphere-Land Study (VOCALS), the
737 Cloud System Evolution over the Trades (CSET), the ObseRvations of CLouds above Aerosols and their
738 intEractionS (ORACLES), and the Aerosol Cloud meTeorology Interactions oVer the western ATlantic
739 Experiment (ACTIVATE). Note that the $ACI_{r, CB}$ values in Figure 6b are also larger than the results from
740 the layer-mean r_c against sub-cloud $N_{CCN, 0.35\%}$, since the layer-mean microphysics is more subject to the
741 cloud droplet evolution processes such as condensational growth and collision-coalescence. The ACI
742 indices from three IOPs are in the ACI range of the previous studies in MBL clouds (Twohy et al., 2005;
743 Lu et al., 2009; Diamond et al., 2018) using aircraft in-situ measurements.

744 To investigate the ACI indices at the upper level of the cloud, the N_c and r_c at the upper cloud
745 ($z_i > 0.8$) are plotted against the above-cloud $N_{CCN, 0.35\%}$ in Figure S5, and the ACI indices are calculated
746 as $ACI_{N, CT}$ and $ACI_{r, CT}$ (denoting the assessments near the cloud top). Compared to the $ACI_{N, CB}$ and
747 $ACI_{r, CB}$, the $ACI_{N, CT}$ and $ACI_{r, CT}$ are much weaker, especially for $ACI_{r, CT}$, as the near cloud top droplets
748 are too large for above-cloud aerosols to exert a significant influence on r_c (Diamond et al., 2018; Gupta
749 et al., 2022). While the weaker cloud top N_c dependence on the $N_{CCN, 0.35\%}$ could be due to the legacy of
750 the sub-cloud CCN impacts on N_c being conveyed to the cloud top. This occurs because FT aerosols and
751 CCN can be entrained down to the MBL before and during the cloud process, as observed in the
752 assessment of inter-cloud cases. These weaker relationships support the notion that although the aerosols

Deleted: though

754 entrained into the upper-cloud region can affect the cloud microphysics to a certain degree, the effects
755 are less pronounced than those from the sub-cloud aerosols (Diamond et al., 2018, Wang et al., 2020)
756 because the MBL cloud N_c and r_c variations are dominated by the condensational growth, collision-
757 coalescence, and entrainment mixing processes near the cloud top.

Deleted: process

Deleted: process

Deleted: cloud top

759 4.2 Precipitation susceptibility

760 The precipitation susceptibility relies on the assessment of relative responses in the precipitation
761 rate to the change in N_c (Feingold and Seibert, 2009; Sorooshian et al., 2009), which is defined as:

$$762 S_o = -\frac{\partial \ln(R_{CB})}{\partial \ln(N_c)}, \quad (10)$$

763 where the R_{CB} is the cloud base precipitation rate calculated in section 2 (equation 5). By incorporating
764 all the cloud cases, including both precipitating and non-precipitating clouds (the R_{CB} can also be
765 calculated based on the drizzle DSD near the cloud base), the S_o accounts for the impact of cloud droplets
766 on the potential precipitation ability of the cloud (Terai et al., 2012).

767 As shown in Figure 7a, the R_{CB} values generally have a negative correlation with increased layer-
768 mean N_c for all three IOPs. The S_o values are 0.979, 1.229, and 1.638, with the absolute values of
769 correlation coefficients being 0.33, 0.29, and 0.45 for SOCRATES, ACE-ENA summer and winter,
770 respectively. These correlation coefficient values fall within the reasonable range found in previous
771 studies on precipitation susceptibility in MBL stratus and stratocumulus clouds (Jung et al., 2016; Gupta
772 et al., 2022), and indicate statistically significant dependences of R_{CB} on N_c . Previous study by Terai et
773 al. (2012) found that the S_o values decrease with the increasing cloud thickness over the southeast Pacific,
774 and Jung et al. (2016) found that the S_o is more pronounced within the medium-deep clouds with
775 thickness ~300-400 m in the MBL stratocumulus over the eastern Pacific. While Gupta et al. (2022)
776 found that the S_o values are generally higher under low ambient N_a condition in the southeastern Atlantic
777 MBL. In this study, R_{CB} for the ACE-ENA winter is more susceptible to the layer-mean N_c than the

781 ACE-ENA summer and SOCRATES, which can be partially attributed to the existence of more large
782 drizzle drops (as shown in Fig. 4d) near the cloud base. As previously discussed, the ACE-ENA winter
783 ~~featured~~ enhanced collision-coalescence and ~~drizzle-recirculating~~ processes, especially under low N_c
784 conditions with more ~~large~~ drizzle drops, leading to the increase of S_o values. In comparison, the higher
785 ambient aerosol and CCN concentrations during SOCRATES lead to relatively narrower drizzle DSDs
786 and may induce effective aerosol buffering effects, where the warm-rain processes in cloud are already
787 fairly suppressed, hence diminishing the sensitivity of R_{CB} to N_c (Stevens and Feingold, 2009; Fan et al.,
788 2020; Gupta et al., 2022).

Deleted: feature with

Deleted: the

Deleted: larger

789 ~~It~~ is well known that the R_{CB} can be parameterized or predicted via an approximate relation with
790 N_c and cloud thickness (H_c), which is usually parameterized in the form of $R_{CB} \propto c H_c^3 N_c^{-1}$ (Lu et al.,
791 2009; Kang et al., 2024). Following the same method, we derive the relationships from three IOPs in
792 Figure 7b, where the R_{CB} are positively (negatively) proportional to the H_c (N_c), with the exponential
793 parameters in the range of the typical values in the MBL clouds (Comstock et al., 2004; vanZanten et al.,
794 2005; Lu et al., 2009). The statistical ~~coefficient of determination (R^2)~~ values of R_{CB} against H_c (N_c) are
795 0.696 (0.177), 0.419 (0.212) and 0.165 (0.295), for the ACE-ENA summer, winter and SOCRATES,
796 respectively, suggesting that the R_{CB} in ACE-ENA clouds may be more determined by H_c , while the
797 R_{CB} in SOCRATES cloud are more related to N_c . Note that the relationship for SOCRATES in this study
798 reveals a similar R_{CB} dependence on N_c but a smaller dependence on the cloud thickness than the study
799 by Kang et al. (2024), who concluded a relationship of $R_{CB} = 1.41 \times 10^{-9} H_c^{3.1} N_c^{-0.8}$, based on the rain
800 rate retrieved from radar and lidar measurements and the aerosol concentration also from the
801 SOCRATES. The discrepancies are possibly due to the different sample selections and different methods
802 in the R_{CB} calculation. Note that the mean cloud thicknesses of the ACE-ENA summer (336.3 m), winter
803 (392.4 m) and SOCRATES (487.4 m), are within the thickness range ~~found to exhibit stronger S_o~~ (Teraï
804 et al., 2012; Jung et al., 2016; Gupta et al., 2022).

Deleted: In addition, it

Deleted:).

Deleted: R^2

Deleted: $73e^{-10} H_c^{3.6} N_c^{-1}$

Deleted: where is

813

814 4.3 Drizzle impacts on sub-cloud CCN and implication to ACI

815 Multiple studies on the MBL clouds have concluded that the in-cloud drizzle formation and
816 evolution processes can effectively impact the sub-cloud CCN budgets via the coalescence-scavenging
817 effect (Wood, 2006; Wood et al., 2012; Diamond et al., 2018; Zheng et al., 2022b; Zhang et al., 2023).
818 Drizzle drops are formed and grow via the collision-coalescence process by collecting cloud droplets and
819 small drizzle drops, resulting in the consumption of CCN (the precursor of cloud droplet), but in the
820 meantime, the in-cloud N_c can be continuously buffered by the sub-cloud CCN replenishment. Although
821 the sub-cloud aerosols (especially in large size) would be added if the drizzle fell and evaporated outside
822 the cloud, the increment cannot compensate for the loss. Therefore, the net result of the whole process is
823 usually presented as the depletion of sub-cloud CCN residuals, and such drizzle modulation on the CCN
824 budget could be substantial in moderate-to-light drizzles or even non-precipitating clouds, depending on
825 the collision-coalescence efficiency (Feingold et al., 1996; Wood, 2006; Kang et al., 2022).

826 The CCN loss rate due to the coalescence-scavenging effect can be calculated as:

$$827 L_{CCN} = -\frac{K H_c}{H_{cp}} * N_c * R_{CB}, \quad (11)$$

828 where the constant K ($2.25 \text{ m}^2 \text{ kg}^{-1}$) denotes the drizzle collection efficiency (Wood et al., 2006; Diamond
829 et al., 2018). H_c is cloud thickness, and H_{cp} is the coupled layer thickness to ensure the change in the
830 cloud layer can be sufficiently conveyed throughout the layer. The calculated CCN loss rate for individual
831 cases is listed in Table S2. Considering all cloud (precipitating cloud) scenarios, the mean CCN loss rates
832 are $-7.69 \pm 13.96 \text{ cm}^{-3}\text{h}^{-1}$ ($-10.45 \pm 15.56 \text{ cm}^{-3}\text{h}^{-1}$), $-6.29 \pm 11.65 \text{ cm}^{-3}\text{h}^{-1}$ ($-12.11 \pm 14.64 \text{ cm}^{-3}\text{h}^{-1}$), and -
833 $4.94 \pm 7.96 \text{ cm}^{-3}\text{h}^{-1}$ ($-5.58 \pm 8.43 \text{ cm}^{-3}\text{h}^{-1}$) for ACE-ENA summer, winter and SOCRATES, respectively.

834 As the results indicate, the ACE-ENA clouds experience more substantial sub-cloud CCN loss than
835 SOCRATES, especially in wintertime precipitating clouds. Recall that the assessment of $ACI_{r,CB}$ relies
836 on the relative changes of r_c and N_{CCN} , while the different L_{CCN} for individual cases can result in the

Deleted: thickness of the

Deleted: ±

Deleted: ±

Deleted:

Deleted: ±

Deleted: ±

Deleted: ±

844 shrinking of the N_{CCN} variation ranges (imagine the abundant CCN are depleted by the coalescence-
845 scavenging). In other words, the given change in r_c corresponds to a narrowed change in N_{CCN} .
846 Mathematically speaking, the assessment of $ACI_{r, CB}$ depends on the ratio of the numerator (change in r_c)
847 and the denominator (change in N_{CCN}). Under the circumstances of substantial cloud-processing to the
848 aerosols, the altered sub-cloud CCN budgets are reflected as a smaller denominator, versus the less
849 altered numerator, hence mathematically presented as an enlarged $ACI_{r, CB}$. Therefore, the coalescence-
850 scavenging effect can not only deplete the sub-cloud CCN, but also quantitatively amplify the assessment
851 of cloud microphysics susceptibilities (Feingold et al., 1999; Duong et al., 2011; Jung et al., 2016; Zheng
852 et al., 2022b). In order to examine the potential impact of the aforementioned processes on the ACI
853 assessment, a sensitivity analysis is conducted by simply retrospectively the sub-cloud $N_{CCN0.35\%}$
854 according to their L_{CCN} . For each retrospective time step ΔT , the r_c values are held unchanged, and the
855 retrospective $N_{CCN0.35\%}$ values for individual cloud cases are given by $N_{CCN0.35\%} - L_{CCN} * \Delta T$, and then
856 the $ACI_{r, CB}$ can be recalculated. Note that assuming a constant r_c value over time inevitably induces
857 uncertainty and biases, as it does not consider the microphysical processes affecting the cloud droplet
858 mean size. However, previous numerical experiments show that the noticeable impact on the cloud mean
859 radius through collision-coalescence necessitates a high degree of CCN depletion, and the quantified
860 percentage changes in droplet mean sizes are several times less than the changes in CCN depletion
861 (Feingold et al., 1996). Hence, the retrospective method, from an observational snapshot point of view,
862 provides a direction that enables the assessment of $ACI_{r, CB}$ as if before the sub-cloud aerosols and CCN
863 are scavenged by in-cloud coalescence-scavenging and precipitation scavenging processes.

864 As shown in Figure 8, the $ACI_{r, CB}$ values tend to decrease with the retrospective time, which
865 indicates the retrospective CCN variation range is enlarged and counteracting the coalescence-
866 scavenging amplification. The detailed illustration of the different $ACI_{r, CB}$ calculated from the scattered
867 r_c and sub-cloud $N_{CCN0.35\%}$ is shown in Figure S6. Note that the $ACI_{r, CB}$ decreasing rates for the

868 precipitating clouds (Fig. 8b) are not as strong as for all clouds because the non-precipitating clouds have
869 smaller L_{CCN} largely due to weaker collision-coalescence. Hence, the ~~retrospective time scale~~ might
870 quickly exceed the actual time of ~~the cloud-processing effects on the aerosol and CCN~~. In other words,
871 the time needed to ~~restore~~ the sub-cloud CCN to the budget before ~~the cloud-processing~~, is shorter. ~~Thus,~~
872 ~~results in the faster decrease of $ACI_{r,CB}$ in the non-precipitating cloud. The~~ retrospective of the sub-cloud
873 CCN budget will yield an alternative assessment of ACI, assuming that the drizzle processes have not
874 yet significantly impacted the sub-cloud CCN budget, especially for the assessment under the
875 precipitating clouds. However, examining the exact precipitating timing is challenging since the aircraft
876 provides a snapshot of the cloud and aerosol information. Thus, this retrospective study only provides a
877 possible direction, and the result should be interpreted with caution.

878

879 5. Summary and Conclusions

880 Based on the aircraft in-situ measurements during ACE-ENA and SOCRATES, the vertical
881 distributions and the evolutions of the aerosol, cloud, and drizzle properties are investigated under the
882 cloud-topped MBL environments. The aerosols and CCN from SOCRATES are the highest among the
883 three IOPs, followed by ACE-ENA summer and winter in descending order in both above- and sub-cloud
884 regimes. The differences can be attributed to the differences in aerosol size distributions between ACE-
885 ENA and SOCRATES, which are largely due to the aerosol sources in those regions. The SOCRATES
886 features the pre-industrial natural environment enriched by aerosols from marine biological productivity
887 and without the contamination of anthropogenic aerosols, while the ACE-ENA features the aerosols from
888 varied sources, including maritime and continental emissions, with distinct seasonal variations.
889 Examining the aerosol size distributions in sub-cloud versus above-cloud regimes manifests the
890 significant influence of cloud processing on aerosols. Physical processing like in-cloud Brownian capture
891 can reduce Aitken mode aerosols, while the chemical processes transform Aitken mode aerosols to larger
892 sizes, moving them toward the accumulation mode. In addition, the in-cloud coalescence processes shift

Deleted: retrospected

Deleted: scale

Deleted: of cloud droplets.

Deleted: store

Deleted: existence

Deleted: Therefore, the

899 sub-cloud aerosol residuals to larger sizes, as multiple aerosols combine into a single aerosol core inside
900 the cloud droplet during collision-coalescence, explaining the observed increase in the tail-end of the
901 aerosol distribution for all IOPs.

902 As for the cloud and drizzle properties, the SOCRATES clouds feature more and smaller cloud
903 droplets than the ACE-ENA summertime and wintertime clouds, with the r_c growths (and percentage
904 increases), from cloud base to top, being $4.03 \mu\text{m}$ (0.66%), $4.78 \mu\text{m}$ (0.68%), and $5.85 \mu\text{m}$ (0.79%) for
905 SOCRATES, ACE-ENA summer, and winter, respectively. The cloud-top entrainment mixing is
906 evidenced in the observed decline of both N_c and LWC_c near the cloud top. The mean cloud-top
907 entrainment rates (w_e) are $0.570 \pm 0.834 \text{ cm s}^{-1}$, $0.581 \pm 0.560 \text{ cm s}^{-1}$, and $0.960 \pm 1.127 \text{ cm s}^{-1}$ for
908 SOCRATES, ACE-ENA summer and winter, respectively. The strongest w_e during ACE-ENA winter is
909 owing to weaker cloud-top inversions and stronger near-cloud-top turbulence. The values of the TKE for
910 three IOPs are generally within the ranges of previous studies (Atlas et al., 2020; Ghate et al., 2021). For
911 drizzle vertical distribution, N_d from the three IOPs all exhibit decreases from cloud top to cloud base,
912 while D_{mod} are in opposite directions with a maximum at the cloud base. The ACE-ENA wintertime
913 clouds feature more prominent drizzle formation and evolution owing to the combined effects of
914 relatively cleaner environment, deeper cloud layer, and slightly stronger in-cloud vertical turbulence,
915 which substantially enhances the collision-coalescence and the drizzle re-circulating processes,
916 compared to the other two IOPs. While satellite retrievals of droplet number concentration heavily rely
917 on the adiabatic cloud assumption and are usually given as a constant of $f_{ad} = 0.8$, the in-situ
918 observational evidence found in this study further confirms the unrealistic nature of this assumption. It
919 will be of interest to utilize multiple aircraft measurements (campaigns) to explore the variability of MBL
920 cloud and drizzle microphysical properties over different marine regions. This can help examine potential
921 predictors for f_{ad} , which will aid in satellite-based retrievals and aerosol-cloud interaction assessments
922 (Painemal and Zuidema, 2011; Grosvenor et al., 2018; Painemal et al., 2021).

923 Comparing the seasonality of cloud base precipitation rate (R_{CB}) during ACE-ENA, more cases
924 with large observed R_{CB} during the winter season, which is consistent with J. Wang et al. (2022). Notably,
925 the sensitivity of R_{CB} to N_c is more pronounced for the ACE-ENA during both winter (with precipitation
926 susceptibility $S_o = 1.638$) and summer ($S_o = 1.229$) compared to the SOCRATES ($S_o = 0.979$). This is
927 partly due to the much higher R_{CB} induced by larger drizzle drops near the cloud base for ACE-ENA, a
928 result of turbulence-driven in-cloud droplet interactions, especially under low N_c condition. Furthermore,
929 R_{CB} can be approximated by a relationship involving N_c and H_c , as suggested in prior research. The
930 relationships established in this study indicate that ACE-ENA clouds, are largely determined by H_c ,
931 while SOCRATES clouds are more influenced by the N_c . The combination of a deeper cloud layer and
932 relatively lower ambient aerosol concentration, eventually leading to stronger drizzle production and
933 evolution during ACE-ENA, especially during the winter season, results in more robust precipitation
934 susceptibility. Note that considering the combined factors of aerosol loadings, cloud morphology and
935 thicknesses, and the assessment methodology, the derived S_o values in this study are generally higher (or
936 close to the upper end) compared to previous studies (Lu et al., 2009; Duong et al., 2011; Terai et al.,
937 2012; Jung et al., 2016; Gupta et al., 2022).

938 The investigations of the ACI via the $ACI_{N, CB}$ and $ACI_{r, CB}$ indices reveal that during the ACE-
939 ENA wintertime, N_c is more sensitive to changes in $N_{CCN0.35\%}$, indicating aerosols more readily activate
940 to become cloud droplets compared to those in the summer, which is consistent with the previous
941 assessment by J. Wang et al. (2022) on the seasonal dependency of the relationship between N_c and
942 aerosols. One influencing factor is the strong dynamic mechanism that speeds up the infusion of CCN
943 into the cloud layer, thus aiding droplet formation. The moderate but statistically significant correlation
944 coefficients between the CCN activation fractions and the TKE agree with a previous study that found
945 the local activation fraction of CCN to be strongly associated with increased updrafts (Hu et al., 2021).
946 Furthermore, the presence of larger aerosols during ACE-ENA winter enhances the droplet activation

Deleted: along with

Deleted: which

Deleted: lead

Deleted: ,

951 process. The SOCRATES IOP highlights a higher $ACI_{r, CB}$, indicating a pronounced decrease in r_c with
952 increasing $N_{CCN0.35\%}$. The $ACI_{r, CB}$ in ACE-ENA is dampened by the presence of more large cloud
953 droplets near the cloud base, particularly under relatively higher $N_{CCN0.35\%}$. However, the combined
954 effect of the relatively cleaner environment and sufficient water vapor results in stronger cloud
955 microphysical responses during the ACE-ENA wintertime than in the summertime. Note that the ACI
956 indices from this study lie in the higher end of the ACI ranges estimated via remote sensing (McComiskey
957 et al., 2009; Dong et al., 2015; Zheng et al., 2022a) possibly because the aircraft assessment of ACI is
958 based on measurements where the aerosols are in direct contact with the cloud layer. Arguably, the
959 assessment of N_c responses to $N_{CCN0.35\%}$ would inevitably be affected by the collision-coalescence
960 process near the cloud base, where simultaneously, the CCN replenishment buffers the N_c and the
961 collision-coalescence process depletes N_c . Hence, finding a layer where these two effects maintain a
962 dynamic balance in N_c might aid in a more accurate assessment and more fundamental understanding of
963 the ACI, which might be revealed by the LES or parcel model simulations.

964 Additionally, the in-cloud drizzle formation and evolution processes significantly influence the
965 sub-cloud CCN budgets via the coalescence-scavenging effect, which can potentially exaggerate the
966 assessment of cloud microphysics susceptibilities. Based on the CCN loss rate (L_{CCN}) from ACE-ENA
967 and SOCRATES, a sensitivity analysis is performed focusing on retrospectively adjusting the sub-cloud
968 CCN according to their L_{CCN} . Results showed that this adjustment led to a decreased $ACI_{r, CB}$,
969 highlighting the significance of the coalescence-scavenging process on the ACI assessment. However,
970 due to the fact that aircraft only provide a snapshot of the clouds and aerosol information, determining
971 the precise drizzle timing for the individual cloud is challenging. Hence, findings from this retrospective
972 approach provide only a direction or theory, and should be taken cautiously. Nevertheless, pursuing
973 further modeling experiments on this matter may be worthwhile. For example, the exact drizzling time
974 could be pinpointed within a model using an Eulerian framework or traced using a Lagrangian framework.

Deleted: larger

976 Nevertheless, the CCN adjustment could more accurately reflect the true characteristics of the cloud and
977 the MBL CCN budget, potentially aiding in a more precise assessment of ACI. Therefore, future works
978 would focus on the model simulation on the MBL clouds from ACE-ENA and SOCRATES and further
979 assess the modeled ACI under the observational constraints, as well as the continuous development of
980 the warm rain microphysical parameterizations, in order to aid in the better represent the MBL clouds in
981 multiple regions.

982

983

984 *Data availability.* The ACE-ENA field campaign data can be accessed from the Department of Energy
985 Atmospheric Radiation Measurement data archive ([https://iop.archive.arm.gov/arm-iop-](https://iop.archive.arm.gov/arm-iop-file/2017/ena/aceena/)
986 [file/2017/ena/aceena/](https://iop.archive.arm.gov/arm-iop-file/2017/ena/aceena/)). The SOCRATES field campaign data are publicly archived on the National
987 Center for Atmospheric Research (NCAR) Earth Observing Laboratory
988 (https://data.eol.ucar.edu/master_lists/generated/socrates/).

989

990 *Author contributions.* The original idea of this study is discussed by XZ, XD, and BX. XZ performed the
991 analyses and wrote the manuscript. XZ, XD, BX, TL, and YW participated in further scientific
992 discussions and provided substantial comments and edits on the paper.

993

994 *Competing interests.* At least one of the (co-)authors is a member of the editorial board of Atmospheric
995 Chemistry and Physics.

996

997 *Acknowledgments.* This work was supported by the NSF grants AGS-2031750/2031751/20211752 at the
998 University of Arizona, Texas A&M University and Stanford University, respectively. The authors
999 sincerely thank the investigators and mentors from the ACE-ENA and SOCRATES field campaigns for
1000 making the data publicly available.

1001 **References.**

- 1002 Albrecht B. A.: Aerosols, Cloud Microphysics, and Fractional Cloudiness, *Science*, 245, 1227-1230,
1003 10.1126/science.245.4923.1227, 1989
- 1004 Albrecht, B. A., Bretherton, C. S., Johnson, D., Scubert, W. H., and Frisch, A. S.: The Atlantic
1005 Stratocumulus Transition Experiment—ASTEX, *B. Am. Meteorol. Soc.*, 76, 889-904,
1006 10.1175/1520-0477(1995)076<0889:Taste>2.0.Co;2, 1995.
- 1007 Albrecht, B., Fang, M., and Ghate, V.: Exploring Stratocumulus Cloud-Top Entrainment Processes and
1008 Parameterizations by Using Doppler Cloud Radar Observations, *J. Atmos. Sci.*, 73, 729-742,
1009 10.1175/JAS-D-15-0147.1, 2016.
- 1010 Atlas, R. L., Bretherton, C. S., Blossey, P. N., Gettelman, A., Bardeen, C., Lin, P., and Ming, Y.: How
1011 Well Do Large-Eddy Simulations and Global Climate Models Represent Observed Boundary Layer
1012 Structures and Low Clouds Over the Summertime Southern Ocean?, *Journal of Advances in
1013 Modeling Earth Systems*, 12, e2020MS002205, <https://doi.org/10.1029/2020MS002205>, 2020.
- 1014 Atlas, R., Mohrmann, J., Finlon, J., Lu, J., Hsiao, I., Wood, R., and Diao, M.: The University of
1015 Washington Ice–Liquid Discriminator (UWILD) improves single-particle phase classifications of
1016 hydrometeors within Southern Ocean clouds using machine learning, *Atmos. Meas. Tech.*, 14,
1017 7079-7101, 10.5194/amt-14-7079-2021, 2021.
- 1018 Baumgardner, D. and Korolev, A.: Airspeed Corrections for Optical Array Probe Sample Volumes, *J.
1019 Atmos. Ocean. Tech.*, 14, 1224-1229, [https://doi.org/10.1175/1520-
1020 0426\(1997\)014<1224:ACFOAP>2.0.CO;2](https://doi.org/10.1175/1520-0426(1997)014<1224:ACFOAP>2.0.CO;2), 1997.
- 1021 Baumgardner, D., Abel, S. J., Axisa, D., Cotton, R., Crosier, J., Field, P., Gurganus, C., Heymsfield, A.,
1022 Korolev, A., Krämer, M., Lawson, P., McFarquhar, G., Ulanowski, Z., and Um, J.: Cloud Ice
1023 Properties: In Situ Measurement Challenges, *Meteor. Monogr.*, 58, 9.1-9.23,
1024 <https://doi.org/10.1175/AMSMONOGRAPHS-D-16-0011.1>, 2017.

1025 Braun, R. A., Dadashazar, H., MacDonald, A. B., Crosbie, E., Jonsson, H. H., Woods, R. K., Flagan, R.
1026 C., Seinfeld, J. H., and Sorooshian, A.: Cloud Adiabaticity and Its Relationship to Marine
1027 Stratocumulus Characteristics Over the Northeast Pacific Ocean, *J. Geophys. Res.-Atmos.*, 123,
1028 13790 - 13806, 10.1029/2018jd029287, 2018.

1029 Brenguier, J. L., Burnet, F., and Geoffroy, O.: Cloud optical thickness and liquid water path – does the k
1030 coefficient vary with droplet concentration?, *Atmos. Chem. Phys.*, 11, 9771-9786, 10.5194/acp-11-
1031 9771-2011, 2011.

1032 Brost, R. A., Wyngaard, J. C., and Lenschow, D. H.: Marine Stratocumulus Layers. Part II: Turbulence
1033 Budgets, *J. Atmos. Sci.*, 39, 818-836, 10.1175/1520-0469(1982)039<0818:MSLPIT>2.0.CO;2,
1034 1982.

1035 Brunke, M. A., Cutler, L., Urzua, R. D., Corral, A. F., Crosbie, E., Hair, J., Hostetler, C., Kirschler, S.,
1036 Larson, V., Li, X.-Y., Ma, P.-L., Minke, A., Moore, R., Robinson, C. E., Scarino, A. J., Schlosser,
1037 J., Shook, M., Sorooshian, A., Lee Thornhill, K., Voigt, C., Wan, H., Wang, H., Winstead, E., Zeng,
1038 X., Zhang, S., and Ziemba, L. D.: Aircraft Observations of Turbulence in Cloudy and Cloud-Free
1039 Boundary Layers Over the Western North Atlantic Ocean From ACTIVATE and Implications for
1040 the Earth System Model Evaluation and Development, *J. Geophys. Res.-Atmos.*, 127,
1041 e2022JD036480, <https://doi.org/10.1029/2022JD036480>, 2022.

1042 Chen, J., Liu, Y., Zhang, M., and Peng, Y.: Height Dependency of Aerosol-Cloud Interaction Regimes,
1043 *J. Geophys. Res.-Atmos.*, 123, 491-506, <https://doi.org/10.1002/2017JD027431>, 2018.

1044 Chen, S., Yau, M. K., and Bartello, P.: Turbulence Effects of Collision Efficiency and Broadening of
1045 Droplet Size Distribution in Cumulus Clouds, *J. Atmos. Sci.*, 75, 203-217,
1046 <https://doi.org/10.1175/JAS-D-17-0123.1>, 2018.

1047 Chen, Y. C., Xue, L., Lebo, Z. J., Wang, H., Rasmussen, R. M., and Seinfeld, J. H.: A comprehensive
1048 numerical study of aerosol-cloud-precipitation interactions in marine stratocumulus, *Atmos. Chem.*
1049 *Phys.*, 11, 9749-9769, 10.5194/acp-11-9749-2011, 2011.

1050 Christensen, M. W., Ma, P. L., Wu, P., Varble, A. C., Mülmenstädt, J., and Fast, J. D.: Evaluation of
1051 aerosol–cloud interactions in E3SM using a Lagrangian framework, *Atmos. Chem. Phys.*, 23, 2789-
1052 2812, 10.5194/acp-23-2789-2023, 2023.

1053 Comstock, K. K., Wood, R., Yuter, S. E., and Bretherton, C. S.: Reflectivity and rain rate in and below
1054 drizzling stratocumulus, *Q. J. R. Meteor. Soc.*, 130, 2891-2918, <https://doi.org/10.1256/qj.03.187>,
1055 2004.

1056 Cooper, W. A., Friesen, R. B., Hayman, M., Jensen, J., Lenschow, D. H., Romashkin, P., Schanot, A., Spuler, S.,
1057 Stith, J., and Wolff, C.: Characterization of Uncertainty in Measurements of Wind from the NSF/NCAR
1058 Gulfstream V Research Aircraft (No. NCAR/TN-528+STR), NCAR Technical Notes,
1059 doi:10.5065/D60G3HJ8, 2016.

1060 Covert, D. S., Kapustin, V. N., Bates, T. S., and Quinn, P. K.: Physical properties of marine boundary
1061 layer aerosol particles of the mid-Pacific in relation to sources and meteorological transport, *J.*
1062 *Geophys. Res.-Atmos.*, 101, 6919-6930, <https://doi.org/10.1029/95JD03068>, 1996.

1063 D'Alessandro, J. J., McFarquhar, G. M., Wu, W., Stith, J. L., Jensen, J. B., and Rauber, R. M.:
1064 Characterizing the Occurrence and Spatial Heterogeneity of Liquid, Ice, and Mixed Phase Low-
1065 Level Clouds Over the Southern Ocean Using in Situ Observations Acquired During SOCRATES,
1066 *J. Geophys. Res.-Atmos.*, 126, e2020JD034482, <https://doi.org/10.1029/2020JD034482>, 2021.

1067 Danker, J., Sourdeval, O., McCoy, I. L., Wood, R., and Possner, A.: Exploring relations between cloud
1068 morphology, cloud phase, and cloud radiative properties in Southern Ocean's stratocumulus clouds,
1069 *Atmos. Chem. Phys.*, 22, 10247-10265, 10.5194/acp-22-10247-2022, 2022.

1070 Desai, N., Liu, Y., Glienke, S., Shaw, R. A., Lu, C., Wang, J., and Gao, S.: Vertical Variation of Turbulent
1071 Entrainment Mixing Processes in Marine Stratocumulus Clouds Using High-Resolution Digital
1072 Holography, *J. Geophys. Res.-Atmos.*, 126, e2020JD033527,
1073 <https://doi.org/10.1029/2020JD033527>, 2021.

1074 Dong, X., Schwantes, A. C., Xi, B., and Wu, P.: Investigation of the marine boundary layer cloud and
1075 CCN properties under coupled and decoupled conditions over the Azores, *J. Geophys. Res.-Atmos.*,
1076 120, 6179-6191, <https://doi.org/10.1002/2014JD022939>, 2015.

1077 Dong, X., X. Zheng, B. Xi, and S. Xie (2023), A Climatology of Midlatitude Maritime Cloud Fraction
1078 and Radiative Effect Derived from the ARM ENA Ground-Based Observations, *J. Climate*, 36(2),
1079 531-546, doi:10.1175/JCLI-D-22-0290.1.

1080 Duong, H. T., Sorooshian, A., and Feingold, G.: Investigating potential biases in observed and modeled
1081 metrics of aerosol-cloud-precipitation interactions, *Atmos. Chem. Phys.*, 11, 4027-4037,
1082 10.5194/acp-11-4027-2011, 2011.

1083 Fan, C., Wang, M., Rosenfeld, D., Zhu, Y., Liu, J., and Chen, B.: Strong Precipitation Suppression by
1084 Aerosols in Marine Low Clouds, *Geophys. Res. Lett.*, 47, e2019GL086207,
1085 <https://doi.org/10.1029/2019GL086207>, 2020.

1086 Feingold, G., Frisch, A. S., Stevens, B., and Cotton, W. R.: On the relationship among cloud turbulence,
1087 droplet formation and drizzle as viewed by Doppler radar, microwave radiometer and lidar, *J.*
1088 *Geophys. Res.-Atmos.*, 104, 22195-22203, <https://doi.org/10.1029/1999JD900482>, 1999.

1089 Feingold, G., Kreidenweis, S. M., Stevens, B., and Cotton, W. R.: Numerical simulations of
1090 stratocumulus processing of cloud condensation nuclei through collision-coalescence, *J. Geophys.*
1091 *Res.-Atmos.*, 101, 21391-21402, <https://doi.org/10.1029/96JD01552>, 1996.

1092 Feingold, G. and McComiskey, A.: ARM's Aerosol-Cloud-Precipitation Research (Aerosol Indirect Effects),
1093 *Meteor. Monogr.*, 57, 22.21-22.15, 10.1175/AMSMONOGRAPHS-D-15-0022.1, 2016.

1094 Feingold, G. and Siebert, H.: Cloud – Aerosol Interactions from the Micro to the Cloud Scale, from the
1095 Strungmann Forum Report, Clouds in the Perturbed Climate System: Their Relationship to Energy
1096 Balance, Atmospheric Dynamics, and Precipitation, 2, edited by: Heintzenberg, J. and Charlson, R.
1097 J., MIT Press, ISBN 978-0-262-01287-4, 2009.

1098 Flossmann, A. I., Hall, W. D., and Pruppacher, H. R.: A Theoretical Study of the Wet Removal of
1099 Atmospheric Pollutants. Part I: The Redistribution of Aerosol Particles Captured through
1100 Nucleation and Impaction Scavenging by Growing Cloud Drops, *J. Atmos. Sci.*, 42, 583-606,
1101 [https://doi.org/10.1175/1520-0469\(1985\)042<0583:ATSOTW>2.0.CO;2](https://doi.org/10.1175/1520-0469(1985)042<0583:ATSOTW>2.0.CO;2), 1985.

1102 Gao, S., Lu, C., Liu, Y., Mei, F., Wang, J., Zhu, L., and Yan, S.: Contrasting Scale Dependence of
1103 Entrainment-Mixing Mechanisms in Stratocumulus Clouds, *Geophys. Res. Lett.*, 47,
1104 e2020GL086970, <https://doi.org/10.1029/2020GL086970>, 2020.

1105 Ghate, V. P. and Cadetdu, M. P.: Drizzle and Turbulence Below Closed Cellular Marine Stratocumulus
1106 Clouds, *J. Geophys. Res.-Atmos.*, 124, 5724-5737, <https://doi.org/10.1029/2018JD030141>, 2019.

1107 Ghate, V. P., Cadetdu, M. P., Zheng, X., and O'Connor, E.: Turbulence in the Marine Boundary Layer
1108 and Air Motions below Stratocumulus Clouds at the ARM Eastern North Atlantic Site, *J. Appl.*
1109 *Meteorol. Clim.*, 60, 1495-1510, 10.1175/JAMC-D-21-0087.1, 2021.

1110 Grabowski, W. W. and Wang, L.-P.: Growth of Cloud Droplets in a Turbulent Environment, *Annual*
1111 *Review of Fluid Mechanics*, 45, 293-324, 10.1146/annurev-fluid-011212-140750, 2013.

1112 Grosvenor, D. P., Sourdeval, O., Zuidema, P., Ackerman, A., Alexandrov, M. D., Bennartz, R., Boers,
1113 R., Cairns, B., Chiu, J. C., Christensen, M., Deneke, H., Diamond, M., Feingold, G., Fridlind, A.,
1114 Hünnerbein, A., Knist, C., Kollias, P., Marshak, A., McCoy, D., Merk, D., Painemal, D., Rausch, J.,
1115 Rosenfeld, D., Russchenberg, H., Seifert, P., Sinclair, K., Stier, P., van Diedenhoven, B., Wendisch,
1116 M., Werner, F., Wood, R., Zhang, Z., and Quaas, J.: Remote Sensing of Droplet Number
1117 Concentration in Warm Clouds: A Review of the Current State of Knowledge and Perspectives,
1118 *Reviews of Geophysics*, 56, 409-453, <https://doi.org/10.1029/2017RG000593>, 2018.

1119 Gupta, S., McFarquhar, G. M., O'Brien, J. R., Delene, D. J., Poellot, M. R., Dobracki, A., Podolske, J.
1120 R., Redemann, J., LeBlanc, S. E., Segal-Rozenhaimer, M., and Pistone, K.: Impact of the variability
1121 in vertical separation between biomass burning aerosols and marine stratocumulus on cloud

1122 microphysical properties over the Southeast Atlantic, *Atmos. Chem. Phys.*, 21, 4615– 4635,
1123 <https://doi.org/10.5194/acp-21-4615-2021>, 2021.

1124 Gupta, S., McFarquhar, G. M., O'Brien, J. R., Poellot, M. R., Delene, D. J., Miller, R. M., and Small
1125 Griswold, J. D.: Factors affecting precipitation formation and precipitation susceptibility of marine
1126 stratocumulus with variable above- and below-cloud aerosol concentrations over the Southeast
1127 Atlantic, *Atmos. Chem. Phys.*, 22, 2769–2793, <https://doi.org/10.5194/acp-22-2769-2022>, 2022.

1128 Hansen, J. E. and Travis, L. D.: Light scattering in planetary atmospheres, *Space Sci. Rev.*, 16, 527-610,
1129 doi:10.1007/BF00168069,1974.

1130 Hill, A. A., Feingold, G., and Jiang, H.: The Influence of Entrainment and Mixing Assumption on
1131 Aerosol–Cloud Interactions in Marine Stratocumulus, *J. Atmos. Sci.*, 66, 1450-1464,
1132 [10.1175/2008JAS2909.1](https://doi.org/10.1175/2008JAS2909.1), 2009.

1133 Hinds, W.C.: *Aerosol Technology, Properties, Behaviour, and Measurement of Airborne Particles*. John
1134 Wiley & Sons Inc., New York., 1999.

1135 Hoffmann, F. and Feingold, G.: A Note on Aerosol Processing by Droplet Collision-Coalescence,
1136 *Geophys. Res. Lett.*, 50, e2023GL103716, <https://doi.org/10.1029/2023GL103716>, 2023.

1137 Hu, A. Z., Igel, A. L., Chuang, P. Y., and Witte, M. K.: Recognition of Inter-Cloud Versus Intra-Cloud
1138 Controls on Droplet Dispersion With Applications to Microphysics Parameterization, *J. Geophys.*
1139 *Res.-Atmos.*, 126, e2021JD035180, <https://doi.org/10.1029/2021JD035180>, 2021.

1140 Hudson, J. G. and Noble, S.: CCN Spectral Shape and Cumulus Cloud and Drizzle Microphysics, *J.*
1141 *Geophys. Res.-Atmos.*, 125, e2019JD031141, <https://doi.org/10.1029/2019JD031141>, 2020.

1142 Jensen, M. P., Ghate, V. P., Wang, D., Apoznanski, D. K., Bartholomew, M. J., Giangrande, S. E.,
1143 Johnson, K. L., and Thieman, M. M.: Contrasting characteristics of open- and closed-cellular
1144 stratocumulus cloud in the eastern North Atlantic, *Atmos. Chem. Phys.*, 21, 14557-14571,
1145 [10.5194/acp-21-14557-2021](https://doi.org/10.5194/acp-21-14557-2021), 2021.

1146 Jones, C. R., Bretherton, C. S., and Leon, D.: Coupled vs. decoupled boundary layers in VOCALS-REX,
1147 Atmos. Chem. Phys., 11, 7143-7153, 10.5194/acp-11-7143-2011, 2011.

1148 Jung, E., Albrecht, B. A., Sorooshian, A., Zuidema, P., and Jonsson, H. H.: Precipitation susceptibility
1149 in marine stratocumulus and shallow cumulus from airborne measurements, Atmos. Chem. Phys.,
1150 16, 11395-11413, 10.5194/acp-16-11395-2016, 2016.

1151 Kang, L., Marchand, R. T., Wood, R., and McCoy, I. L.: Coalescence Scavenging Drives Droplet
1152 Number Concentration in Southern Ocean Low Clouds, Geophys. Res. Lett., 49, e2022GL097819,
1153 <https://doi.org/10.1029/2022GL097819>, 2022.

1154 Kang, L., Marchand, R. T., and Wood, R.: Stratocumulus Precipitation Properties Over the Southern
1155 Ocean Observed From Aircraft During the SOCRATES Campaign, J. Geophys. Res.-Atmos., 129,
1156 e2023JD039831, <https://doi.org/10.1029/2023JD039831>, 2024.

1157 Kim, S. H., Kim, J., Kim, J. H., and Chun, H. Y.: Characteristics of the derived energy dissipation rate
1158 using the 1 Hz commercial aircraft quick access recorder (QAR) data, Atmos. Meas. Tech.,
1159 15, 2277-2298, 10.5194/amt-15-2277-2022, 2022.

1160 Lang, F., Ackermann, L., Huang, Y., Truong, S. C. H., Siems, S. T., and Manton, M. J.: A climatology
1161 of open and closed mesoscale cellular convection over the Southern Ocean derived from Himawari-
1162 8 observations, Atmos. Chem. Phys., 22, 2135-2152, 10.5194/acp-22-2135-2022, 2022.

1163 Lu, C., Zhu, L., Liu, Y., Mei, F., Fast, J. D., Pekour, M. S., Luo, S., Xu, X., He, X., Li, J., and Gao, S.:
1164 Observational study of relationships between entrainment rate, homogeneity of mixing, and cloud
1165 droplet relative dispersion, Atmos. Res., 293, 106900,
1166 <https://doi.org/10.1016/j.atmosres.2023.106900>, 2023.

1167 Lu, M.-L., Sorooshian, A., Jonsson, H. H., Feingold, G., Flagan, R. C., and Seinfeld, J. H.: Marine
1168 stratocumulus aerosol-cloud relationships in the MASE-II experiment: Precipitation susceptibility
1169 in eastern Pacific marine stratocumulus, J. Geophys. Res.-Atmos., 114,
1170 <https://doi.org/10.1029/2009JD012774>, 2009.

1171 Mann, J. A. L., Christine Chiu, J., Hogan, R. J., O'Connor, E. J., L'Ecuyer, T. S., Stein, T. H. M., and
1172 Jefferson, A.: Aerosol impacts on drizzle properties in warm clouds from ARM Mobile Facility
1173 maritime and continental deployments, *J. Geophys. Res.-Atmos.*, 119, 4136-4148,
1174 <https://doi.org/10.1002/2013JD021339>, 2014.

1175 [Marcovecchio, A. R., Xi, B., Zheng, X., Wu, P., Dong, X., and Behrangi, A.: What Are the Similarities](https://doi.org/10.1029/2022JD037109)
1176 [and Differences in Marine Boundary Layer Cloud and Drizzle Microphysical Properties During the](https://doi.org/10.1029/2022JD037109)
1177 [ACE-ENA and MARCUS Field Campaigns?](https://doi.org/10.1029/2022JD037109), *J. Geophys. Res.-Atmos.*, 128, e2022JD037109,
1178 <https://doi.org/10.1029/2022JD037109>, 2023.

1179 Mechem, D. B., Wittman, C. S., Miller, M. A., Yuter, S. E., and de Szoeke, S. P.: Joint Synoptic and
1180 Cloud Variability over the Northeast Atlantic near the Azores, *J. Appl. Meteorol. Clim.*, 57, 1273-
1181 1290, <https://doi.org/10.1175/JAMC-D-17-0211.1>, 2018.

1182 McComiskey, A., Feingold, G., Frisch, A. S., Turner, D. D., Miller, M. A., Chiu, J. C., Min, Q., and
1183 Ogren, J. A.: An assessment of aerosol-cloud interactions in marine stratus clouds based on surface
1184 remote sensing, *J. Geophys. Res.-Atmos.*, 114, <https://doi.org/10.1029/2008JD011006>, 2009.

1185 McCoy, I. L., Wood, R., and Fletcher, J. K.: Identifying Meteorological Controls on Open and Closed
1186 Mesoscale Cellular Convection Associated with Marine Cold Air Outbreaks, *J. Geophys. Res.-*
1187 *Atmos.*, 122, 11,678-611,702, <https://doi.org/10.1002/2017JD027031>, 2017.

1188 McCoy, I. L., McCoy, D. T., Wood, R., Regayre, L., Watson-Parris, D., Grosvenor, D. P., Mulcahy, J.
1189 P., Hu, Y., Bender, F. A. M., Field, P. R., Carslaw, K. S., and Gordon, H.: The hemispheric contrast
1190 in cloud microphysical properties constrains aerosol forcing, *P. Natl. Acad. Sci. USA*, 117, 18998-
1191 19006, [10.1073/pnas.1922502117](https://doi.org/10.1073/pnas.1922502117), 2020.

1192 McCoy, I. L., Bretherton, C. S., Wood, R., Twohy, C. H., Gettelman, A., Bardeen, C. G., and Toohey,
1193 D. W.: Influences of Recent Particle Formation on Southern Ocean Aerosol Variability and Low
1194 Cloud Properties, *J. Geophys. Res.-Atmos.*, 126, e2020JD033529,
1195 <https://doi.org/10.1029/2020JD033529>, 2021.

1196 McFarquhar, G. M., Bretherton, C. S., Marchand, R., Protat, A., DeMott, P. J., Alexander, S. P., Roberts,
1197 G. C., Twohy, C. H., Toohey, D., Siems, S., Huang, Y., Wood, R., Rauber, R. M., Lasher-Trapp,
1198 S., Jensen, J., Stith, J. L., Mace, J., Um, J., Järvinen, E., Schnaiter, M., Gettelman, A., Sanchez, K.
1199 J., McCluskey, C. S., Russell, L. M., McCoy, I. L., Atlas, R. L., Bardeen, C. G., Moore, K. A., Hill,
1200 T. C. J., Humphries, R. S., Keywood, M. D., Ristovski, Z., Cravigan, L., Schofield, R., Fairall, C.,
1201 Mallet, M. D., Kreidenweis, S. M., Rainwater, B., D'Alessandro, J., Wang, Y., Wu, W., Saliba, G.,
1202 Levin, E. J. T., Ding, S., Lang, F., Truong, S. C. H., Wolff, C., Haggerty, J., Harvey, M. J.,
1203 Klekociuk, A. R., and McDonald, A.: Observations of Clouds, Aerosols, Precipitation, and Surface
1204 Radiation over the Southern Ocean: An Overview of CAPRICORN, MARCUS, MICRE, and
1205 SOCRATES, *B. Am. Meteorol. Soc.*, 102, E894-E928, [https://doi.org/10.1175/BAMS-D-20-](https://doi.org/10.1175/BAMS-D-20-0132.1)
1206 0132.1, 2021.

1207 Muñoz-Esparza, D., Sharman, R. D., and Lundquist, J. K.: Turbulence Dissipation Rate in the
1208 Atmospheric Boundary Layer: Observations and WRF Mesoscale Modeling during the XPIA Field
1209 Campaign, *Mon. Weather Rev.*, 146, 351-371, <https://doi.org/10.1175/MWR-D-17-0186.1>, 2018.

1210 Olfert, J. S., Kulkarni, P., and Wang, J.: Measuring aerosol size distributions with the fast integrated
1211 mobility spectrometer, *Journal of Aerosol Science*, 39, 940-956,
1212 <https://doi.org/10.1016/j.jaerosci.2008.06.005>, 2008.

1213 Painemal, D. and Zuidema, P.: Assessment of MODIS cloud effective radius and optical thickness
1214 retrievals over the Southeast Pacific with VOCALS-REx in situ measurements, *J. Geophys. Res.-*
1215 *Atmos.*, 116, <https://doi.org/10.1029/2011JD016155>, 2011.

1216 Painemal, D., Chang, F. L., Ferrare, R., Burton, S., Li, Z., Smith Jr, W. L., Minnis, P., Feng, Y., and
1217 Clayton, M.: Reducing uncertainties in satellite estimates of aerosol–cloud interactions over the
1218 subtropical ocean by integrating vertically resolved aerosol observations, *Atmos. Chem. Phys.*, 20,
1219 7167-7177, [10.5194/acp-20-7167-2020](https://doi.org/10.5194/acp-20-7167-2020), 2020.

1220 Painemal, D., Spangenberg, D., Smith Jr, W. L., Minnis, P., Cairns, B., Moore, R. H., Crosbie, E.,
1221 Robinson, C., Thornhill, K. L., Winstead, E. L., and Ziemba, L.: Evaluation of satellite retrievals of
1222 liquid clouds from the GOES-13 imager and MODIS over the midlatitude North Atlantic during the
1223 NAAMES campaign, *Atmos. Meas. Tech.*, 14, 6633-6646, 10.5194/amt-14-6633-2021, 2021.

1224 Pinsky, M. B. and Khain, A. P.: Turbulence effects on droplet growth and size distribution in clouds—
1225 A review, *Journal of Aerosol Science*, 28, 1177-1214, [https://doi.org/10.1016/S0021-](https://doi.org/10.1016/S0021-8502(97)00005-0)
1226 8502(97)00005-0, 1997.

1227 Pruppacher, H. R. and Klett, J. D.: *Microphysics of clouds and precipitation*, Kluwer Academic
1228 Publishers, Dordrecht, the Netherlands, 1997.

1229 Rémillard, J. and Tselioudis, G.: Cloud Regime Variability over the Azores and Its Application to
1230 Climate Model Evaluation, *J. Climate*, 28, 9707-9720, <https://doi.org/10.1175/JCLI-D-15-0066.1>,
1231 2015.

1232 Sanchez, K. J., Roberts, G. C., Diao, M., and Russell, L. M.: Measured Constraints on Cloud Top
1233 Entrainment to Reduce Uncertainty of Nonprecipitating Stratocumulus Shortwave Radiative
1234 Forcing in the Southern Ocean, *Geophys. Res. Lett.*, 47, e2020GL090513,
1235 <https://doi.org/10.1029/2020GL090513>, 2020.

1236 Sanchez, K. J., Roberts, G. C., Saliba, G., Russell, L. M., Twohy, C., Reeves, J. M., Humphries, R. S.,
1237 Keywood, M. D., Ward, J. P., and McRobert, I. M.: Measurement report: Cloud processes and the
1238 transport of biological emissions affect southern ocean particle and cloud condensation nuclei
1239 concentrations, *Atmos. Chem. Phys.*, 21, 3427-3446, 10.5194/acp-21-3427-2021, 2021.

1240 Siebert, H., Shaw, R. A., and Warhaft, Z.: Statistics of Small-Scale Velocity Fluctuations and Internal
1241 Intermittency in Marine Stratocumulus Clouds, *J. Atmos. Sci.*, 67, 262-273,
1242 <https://doi.org/10.1175/2009JAS3200.1>, 2010.

Moved down [1]: Stevens, B. and Feingold, G.: Untangling aerosol effects on clouds and precipitation in a buffered system, *Nature*, 461, 607-613, 10.1038/nature08281, 2009.¶

1246 [Smalley, M. A., Witte, M. K., Jeong, J.-H., and Chinita, M. J.: A climatology of cold pools distinct from](#)
1247 [background turbulence at the Eastern North Atlantic observations site, EGU sphere \[preprint\],](#)
1248 <https://doi.org/10.5194/egusphere-2024-1098>, 2024.

1249 [Stevens, B. and Feingold, G.: Untangling aerosol effects on clouds and precipitation in a buffered system,](#)
1250 [Nature](#), 461, 607-613, 10.1038/nature08281, 2009.

1251 Sorooshian, A., Feingold, G., Lebsock, M. D., Jiang, H., and Stephens, G. L.: On the precipitation
1252 susceptibility of clouds to aerosol perturbations, *Geophys. Res. Lett.*, 36,
1253 <https://doi.org/10.1029/2009GL038993>, 2009.

1254 [Su, T., Li, Z., Henao, N. R., Luan, Q., and Yu, F.: Constraining effects of aerosol-cloud interaction by](#)
1255 [accounting for coupling between cloud and land surface, *Science Advances*, 10, ead15044,](#)
1256 [10.1126/sciadv.ad15044](https://doi.org/10.1126/sciadv.ad15044),

1257 Terai, C. R. and Wood, R.: Aircraft observations of cold pools under marine stratocumulus, *Atmos.*
1258 *Chem. Phys.*, 13, 9899-9914, 10.5194/acp-13-9899-2013, 2013.

1259 Terai, C. R., Wood, R., Leon, D. C., and Zuidema, P.: Does precipitation susceptibility vary with
1260 increasing cloud thickness in marine stratocumulus?, *Atmos. Chem. Phys.*, 12, 4567-4583,
1261 10.5194/acp-12-4567-2012, 2012.

1262 Twohy, C. H., Petters, M. D., Snider, J. R., Stevens, B., Tahnk, W., Wetzel, M., Russell, L., and Burnet,
1263 F.: Evaluation of the aerosol indirect effect in marine stratocumulus clouds: Droplet number, size,
1264 liquid water path, and radiative impact, *J. Geophys. Res.-Atmos.*, 110,
1265 <https://doi.org/10.1029/2004JD005116>, 2005.

1266 vanZanten, M. C., Stevens, B., Vali, G., and Lenschow, D. H.: Observations of Drizzle in Nocturnal
1267 Marine Stratocumulus, *J. Atmos. Sci.*, 62, 88-106, <https://doi.org/10.1175/JAS-3355.1>, 2005.

1268 Waclawczyk, M., Ma, Y. F., Kopeć, J. M., and Malinowski, S. P.: Novel approaches to estimating the
1269 turbulent kinetic energy dissipation rate from low- and moderate-resolution velocity fluctuation
1270 time series, *Atmos. Meas. Tech.*, 10, 4573-4585, 10.5194/amt-10-4573-2017, 2017.

Moved (insertion) [1]

1271 Wang, J., Wood, R., Jensen, M. P., Chiu, J. C., Liu, Y., Lamer, K., Desai, N., Giangrande, S. E., Knopf,
1272 D. A., Kollias, P., Laskin, A., Liu, X., Lu, C., Mechem, D., Mei, F., Starzec, M., Tomlinson, J.,
1273 Wang, Y., Yum, S. S., Zheng, G., Aiken, A. C., Azevedo, E. B., Blanchard, Y., China, S., Dong,
1274 X., Gallo, F., Gao, S., Ghate, V. P., Glienke, S., Goldberger, L., Hardin, J. C., Kuang, C., Luke, E.
1275 P., Matthews, A. A., Miller, M. A., Moffet, R., Pekour, M., Schmid, B., Sedlacek, A. J., Shaw, R.
1276 A., Shilling, J. E., Sullivan, A., Suski, K., Veghte, D. P., Weber, R., Wyant, M., Yeom, J.,
1277 Zawadowicz, M., and Zhang, Z.: Aerosol and Cloud Experiments in the Eastern North Atlantic
1278 (ACE-ENA), *B. Am. Meteorol. Soc.*, 103, E619-E641, 10.1175/BAMS-D-19-0220.1, 2022.

1279 Wang, Y., Zhao, C., McFarquhar, G. M., Wu, W., Reeves, M., and Li, J.: Dispersion of Droplet Size
1280 Distributions in Supercooled Non-precipitating Stratocumulus from Aircraft Observations Obtained
1281 during the Southern Ocean Cloud Radiation Aerosol Transport Experimental Study, *J. Geophys.*
1282 *Res.-Atmos.*, 126, e2020JD033720, <https://doi.org/10.1029/2020JD033720>, 2021a.

1283 Wang, Y., Zheng, G., Jensen, M. P., Knopf, D. A., Laskin, A., Matthews, A. A., Mechem, D., Mei, F.,
1284 Moffet, R., Sedlacek, A. J., Shilling, J. E., Springston, S., Sullivan, A., Tomlinson, J., Veghte, D.,
1285 Weber, R., Wood, R., Zawadowicz, M. A., and Wang, J.: Vertical profiles of trace gas and aerosol
1286 properties over the eastern North Atlantic: variations with season and synoptic condition, *Atmos.*
1287 *Chem. Phys.*, 21, 11079-11098, 10.5194/acp-21-11079-2021, 2021b.

1288 Wang, Y., Zheng, X., Dong, X., Xi, B., Wu, P., Logan, T., and Yung, Y. L.: Impacts of long-range
1289 transport of aerosols on marine-boundary-layer clouds in the eastern North Atlantic, *Atmos. Chem.*
1290 *Phys.*, 20, 14741-14755, 10.5194/acp-20-14741-2020, 2020.

1291 Wang, Y., Zheng, X., Dong, X., Xi, B., and Yung, Y. L.: Insights of warm-cloud biases in Community
1292 Atmospheric Model 5 and 6 from the single-column modeling framework and Aerosol and Cloud
1293 Experiments in the Eastern North Atlantic (ACE-ENA) observations, *Atmos. Chem. Phys.*, 23,
1294 8591-8605, 10.5194/acp-23-8591-2023, 2023.

1295 Wallace, J. M. and Hobbs, P. V.: Atmospheric Science: An Introductory Survey, 2nd edn., Academic
1296 Press/Elsevier, 483 pp, 2006.

1297 Witte, M. K., Chuang, P. Y., Ayala, O., Wang, L.-P., and Feingold, G.: Comparison of Observed and
1298 Simulated Drop Size Distributions from Large-Eddy Simulations with Bin Microphysics, *Mon.*
1299 *Weather Rev.*, 147, 477-493, <https://doi.org/10.1175/MWR-D-18-0242.1>, 2019.

1300 Wood, R.: Drizzle in Stratiform Boundary Layer Clouds. Part I: Vertical and Horizontal Structure, *J.*
1301 *Atmos. Sci.*, 62, 3011-3033, 10.1175/JAS3529.1, 2005.

1302 Wood, R.: Rate of loss of cloud droplets by coalescence in warm clouds, *J. Geophys. Res.-Atmos.*, 111,
1303 <https://doi.org/10.1029/2006JD007553>, 2006.

1304 Wood, R., Wyant, M., Bretherton, C. S., Rémillard, J., Kollias, P., Fletcher, J., Stemmler, J., de Szoeker,
1305 S., Yuter, S., Miller, M., Mechem, D., Tselioudis, G., Chiu, J. C., Mann, J. A. L., O'Connor, E. J.,
1306 Hogan, R. J., Dong, X., Miller, M., Ghate, V., Jefferson, A., Min, Q., Minnis, P., Palikonda, R.,
1307 Albrecht, B., Luke, E., Hannay, C., and Lin, Y.: Clouds, Aerosols, and Precipitation in the Marine
1308 Boundary Layer: An Arm Mobile Facility Deployment, *B. Am. Meteorol. Soc.*, 96, 419-440,
1309 10.1175/BAMS-D-13-00180.1, 2015.

1310 Wu, P., Dong, X., and Xi, B.: A Climatology of Marine Boundary Layer Cloud and Drizzle Properties
1311 Derived from Ground-Based Observations over the Azores, *J. Climate*, 33, 10133-10148,
1312 10.1175/JCLI-D-20-0272.1, 2020.

1313 Wu, P., Dong, X., Xi, B., Liu, Y., Thieman, M., and Minnis, P.: Effects of environment forcing on marine
1314 boundary layer cloud-drizzle processes, *J. Geophys. Res.-Atmos.*, 122, 4463-4478,
1315 <https://doi.org/10.1002/2016JD026326>, 2017.

1316 Wyant, M. C., Bretherton, C. S., Wood, R., Blossey, P. N., and McCoy, I. L.: High Free-Tropospheric
1317 Aitken-Mode Aerosol Concentrations Buffer Cloud Droplet Concentrations in Large-Eddy
1318 Simulations of Precipitating Stratocumulus, *Journal of Advances in Modeling Earth Systems*, 14,
1319 e2021MS002930, <https://doi.org/10.1029/2021MS002930>, 2022.

1320 Yeom, J. M., Yum, S. S., Shaw, R. A., La, I., Wang, J., Lu, C., Liu, Y., Mei, F., Schmid, B., and
1321 Matthews, A.: Vertical Variations of Cloud Microphysical Relationships in Marine Stratocumulus
1322 Clouds Observed During the ACE-ENA Campaign, *J. Geophys. Res.-Atmos.*, 126,
1323 e2021JD034700, <https://doi.org/10.1029/2021JD034700>, 2021.

1324 Zawadowicz, M. A., Suski, K., Liu, J., Pekour, M., Fast, J., Mei, F., Sedlacek, A. J., Springston, S.,
1325 Wang, Y., Zaveri, R. A., Wood, R., Wang, J., and Shilling, J. E.: Aircraft measurements of aerosol
1326 and trace gas chemistry in the eastern North Atlantic, *Atmos. Chem. Phys.*, 21, 7983-8002,
1327 10.5194/acp-21-7983-2021, 2021.

1328 Zhang, J., Zhou, X., Goren, T., and Feingold, G.: Albedo susceptibility of northeastern Pacific
1329 stratocumulus: the role of covarying meteorological conditions, *Atmos. Chem. Phys.*, 22, 861-880,
1330 10.5194/acp-22-861-2022, 2022.

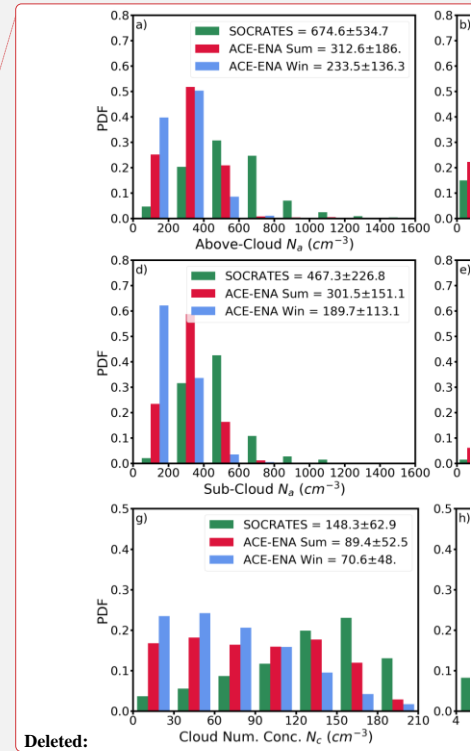
1331 Zhang, X., Dong, X., Xi, B., and Zheng, X.: Aerosol Properties and Their Influences on Marine Boundary
1332 Layer Cloud Condensation Nuclei over the Southern Ocean, *Atmosphere-Basel*, 14,
1333 10.3390/atmos14081246, 2023.

1334 Zheng, G., Wang, Y., Aiken, A. C., Gallo, F., Jensen, M. P., Kollias, P., Kuang, C., Luke, E., Springston,
1335 S., Uin, J., Wood, R., and Wang, J.: Marine boundary layer aerosol in the eastern North Atlantic:
1336 seasonal variations and key controlling processes, *Atmos. Chem. Phys.*, 18, 17615-17635,
1337 10.5194/acp-18-17615-2018, 2018.

1338 Zheng, G., Wang, Y., Wood, R., Jensen, M. P., Kuang, C., McCoy, I. L., Matthews, A., Mei, F.,
1339 Tomlinson, J. M., Shilling, J. E., Zawadowicz, M. A., Crosbie, E., Moore, R., Ziemba, L., Andreae,
1340 M. O., and Wang, J.: New particle formation in the remote marine boundary layer, *Nature*
1341 *Communications*, 12, 527, 10.1038/s41467-020-20773-1, 2021.

1342 Zheng, X., Dong, X., Ward, D. M., Xi, B., Wu, P., and Wang, Y.: Aerosol-Cloud-Precipitation
1343 Interactions in a Closed-cell and Non-homogenous MBL Stratocumulus Cloud, *Adv. Atmos. Sci.*,
1344 39, 2107-2123, 10.1007/s00376-022-2013-6, 2022a.

1345 Zheng, X., Xi, B., Dong, X., Wu, P., Logan, T., and Wang, Y.: Environmental effects on aerosol–cloud
 1346 interaction in non-precipitating marine boundary layer (MBL) clouds over the eastern North
 1347 Atlantic, *Atmos. Chem. Phys.*, 22, 335-354, 10.5194/acp-22-335-2022, 2022b.
 1348 Zuidema, P., Torri, G., Muller, C., and Chandra, A.: A Survey of Precipitation-Induced Atmospheric
 1349 Cold Pools over Oceans and Their Interactions with the Larger-Scale Environment, *Surveys in*
 1350 *Geophysics*, 38, 1283-1305, 10.1007/s10712-017-9447-x, 2017.



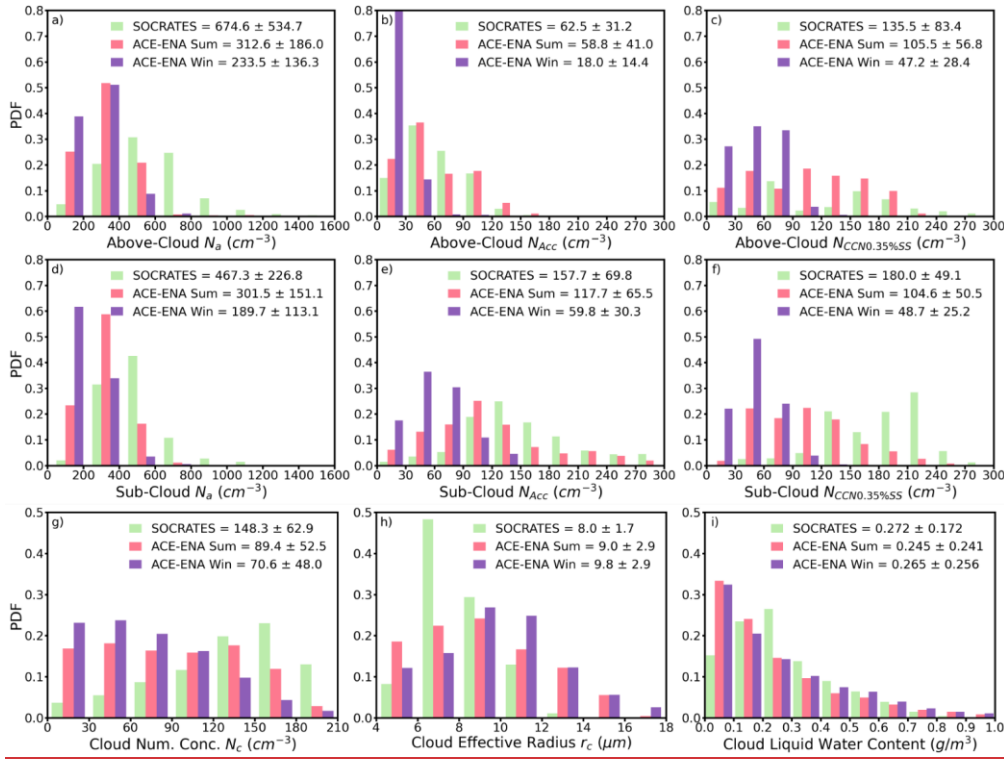


Figure 1. Probability Density Functions (PDFs) of N_a , N_{ACC} and $N_{CCN0.35\%}$ in the above-cloud (a, b, c) and sub-cloud (d, e, f) regimes; and the cloud microphysical properties of N_c (g), r_c (h), and LWC_c (f) within cloud layer. The statistical metrics in the legends denote the mean and standard deviation values for all samples in three IOPs. The ACE-ENA summer, winter and SOCRATES are color-coded with pink, purple and green, respectively.

Deleted: red, blue

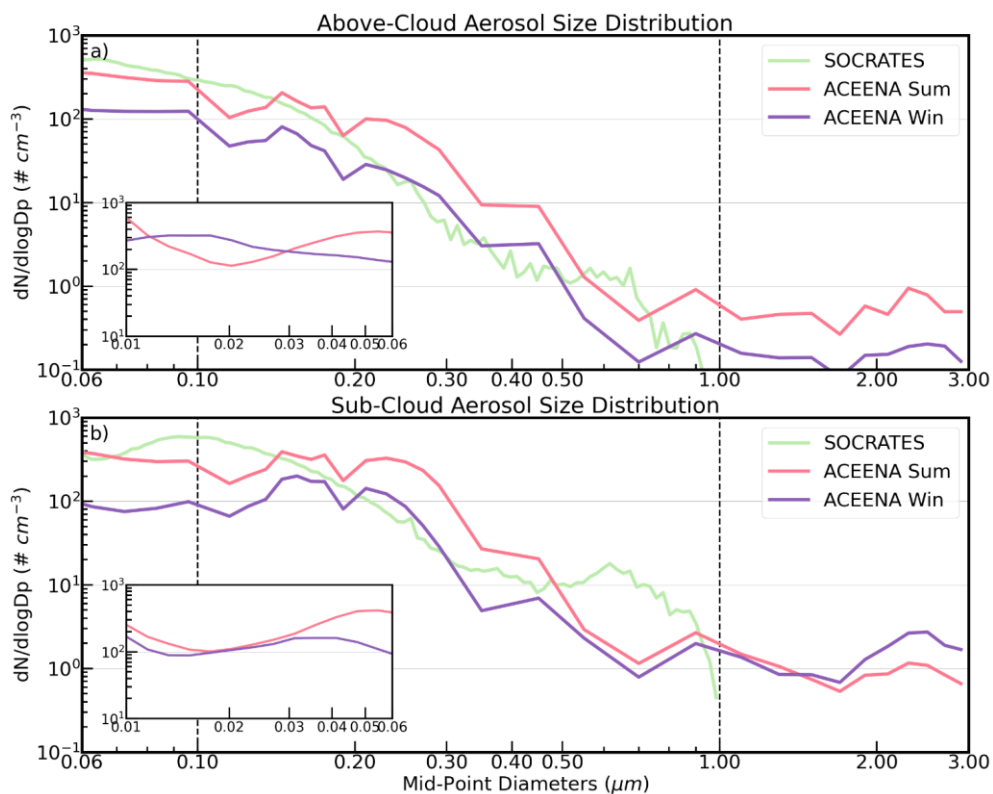
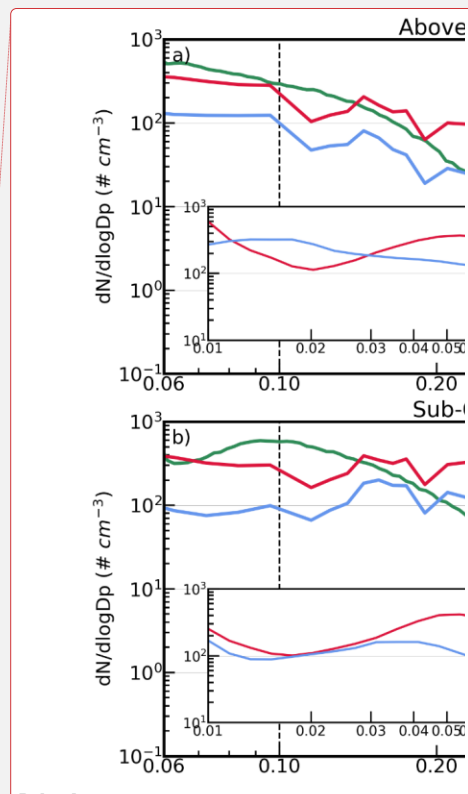
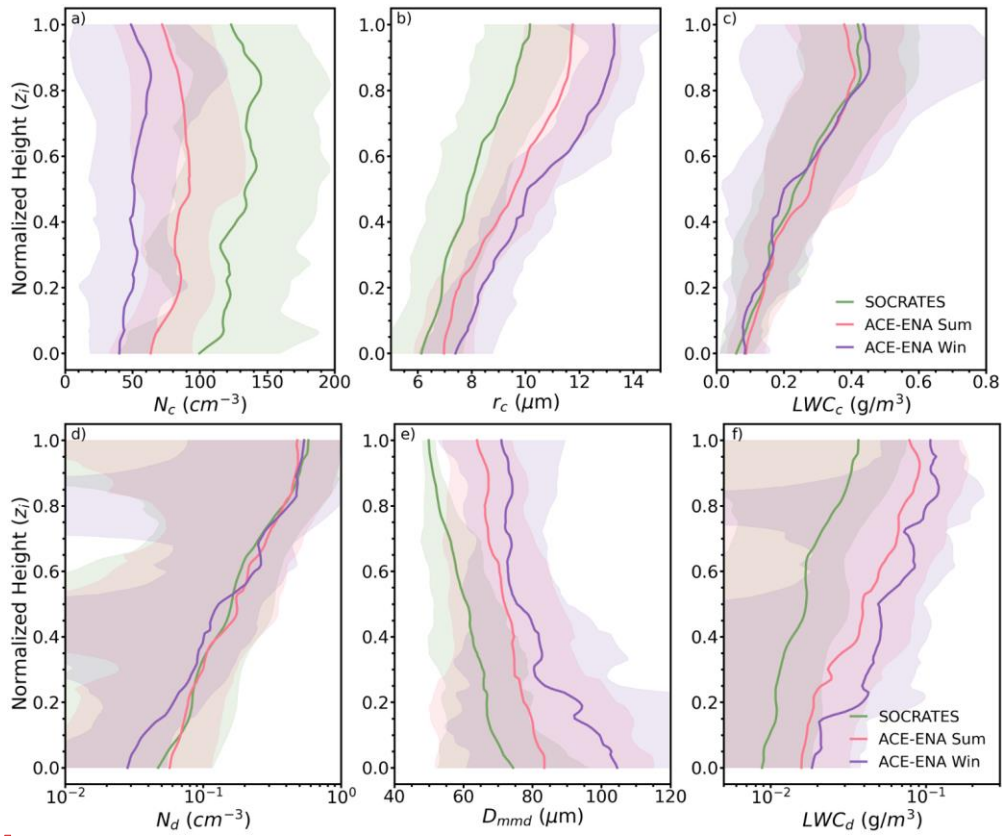


Figure 2. Aerosol size distributions ($D_p = 0.06 - 3 \mu\text{m}$) for above-cloud (a) and sub-cloud (b) regimes. The vertical dashed line at $D_p = 0.1 \mu\text{m}$ and at $D_p = 1 \mu\text{m}$ denotes the demarcations between Accumulation mode, Aitken mode and Coarse mode aerosols. The inner plots denote a smaller range of Aitken mode size distribution ($D_p = 0.01 - 0.06 \mu\text{m}$) available from ACE-ENA. The ACE-ENA summer, winter and SOCRATES are color-coded with pink, purple and green, respectively.

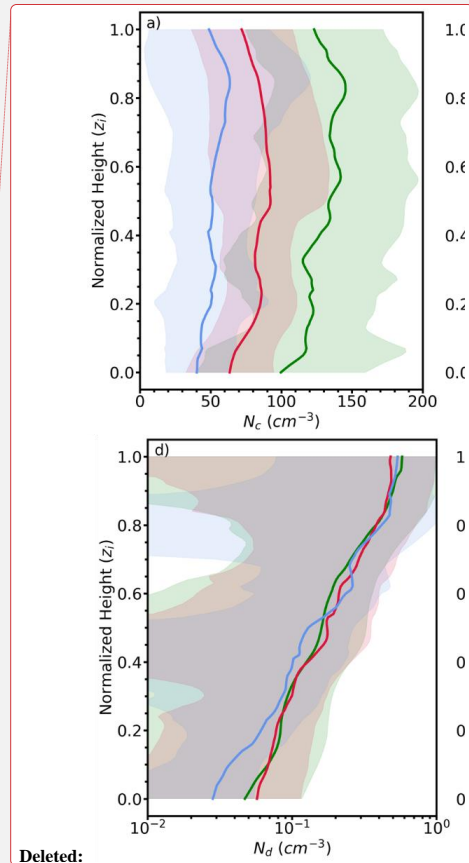


Deleted:

Deleted: red, blue

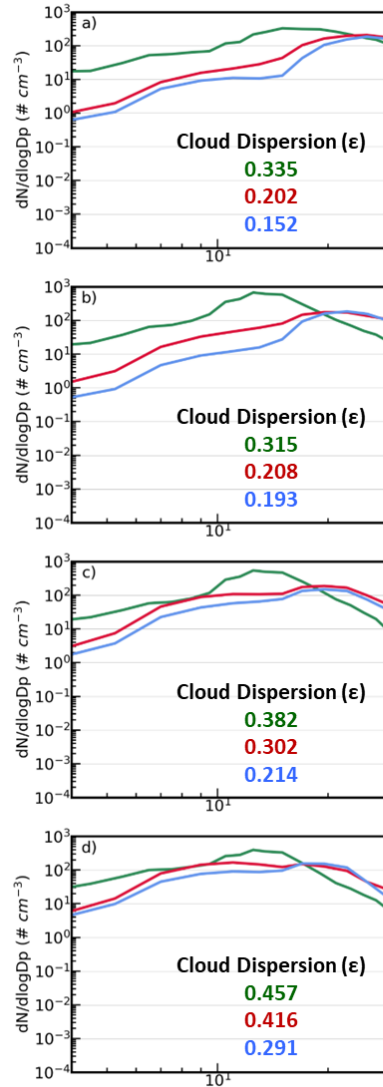
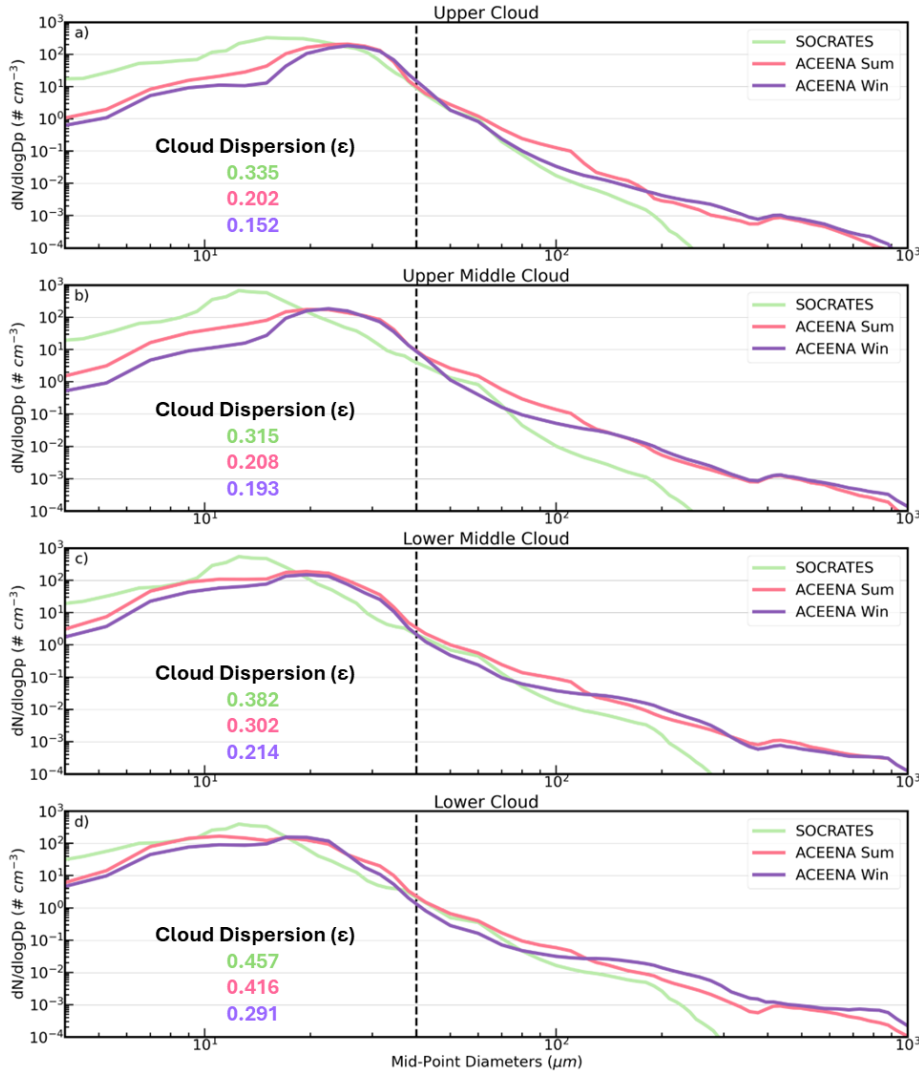


1351 **Figure 3.** Vertical distributions of N_c (a), r_c (b), LWC_c (c), N_d (d), D_{mmd} (e), and LWC_d (f). Here the
 1352 $z_i = 0$ denotes cloud base and $z_i = 1$ denotes cloud top. Shaded areas denote the inter-cloud-case
 1353 standard deviations. The ACE-ENA summer, winter and SOCRATES are color-coded with pink, purple
 1354 and green, respectively.



Deleted:

Deleted: red, blue



Deleted:

Deleted: red, blue

1356 **Figure 4.** Cloud and drizzle size distributions for a) upper cloud ($z_i > 0.8$), b) upper-middle cloud ($0.5 \leq$
 1357 $z_i < 0.8$), c) lower-middle cloud ($0.2 \leq z_i < 0.5$) and d) lower cloud ($z_i < 0.2$). The vertical dashed
 1358 line at $D_p = 40 \mu\text{m}$ denotes the demarcation between cloud droplets and drizzle drops. The ACE-ENA
 1359 summer, winter and SOCRATES are color-coded with ~~pink, purple~~ and green, respectively.

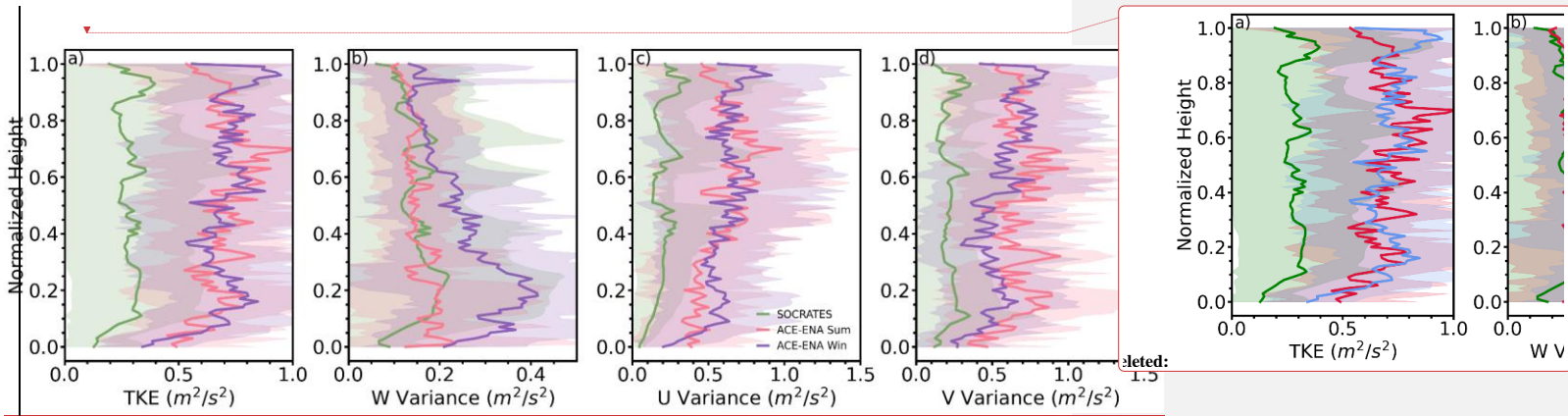


Figure 5. Vertical distributions of in-cloud TKE (a), w'^2 (b), u'^2 (c) and v'^2 (d). Shaded areas denote the inter-cloud-case standard deviations. The ACE-ENA summer, winter and SOCRATES are color-coded with pink, purple and green, respectively.

Deleted: red, blue

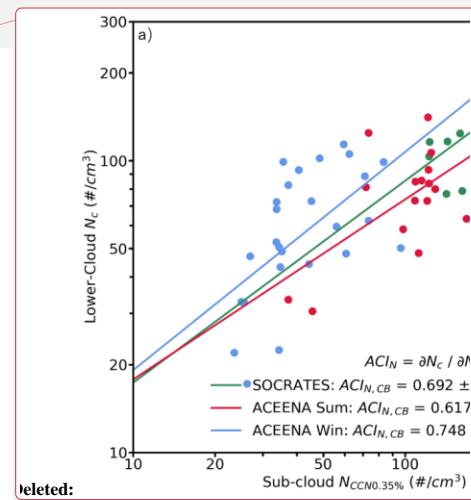
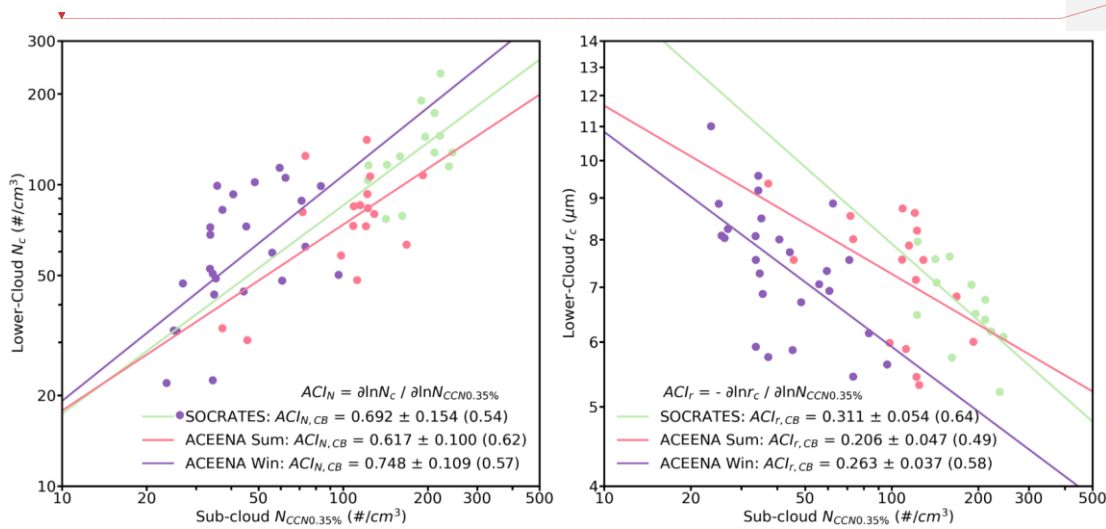


Figure 6. Scatterplots of the a) N_c and b) r_c at the lower-cloud ($z_i < 0.2$) against the sub-cloud $N_{CCN0.35\%}$. The statistical metrics in the legends denote the ACI values and standard errors, and the absolute values of correlation coefficients (in parentheses). The ACE-ENA summer, winter and SOCRATES are color-coded with pink, purple and green, respectively.

Deleted: red, blue

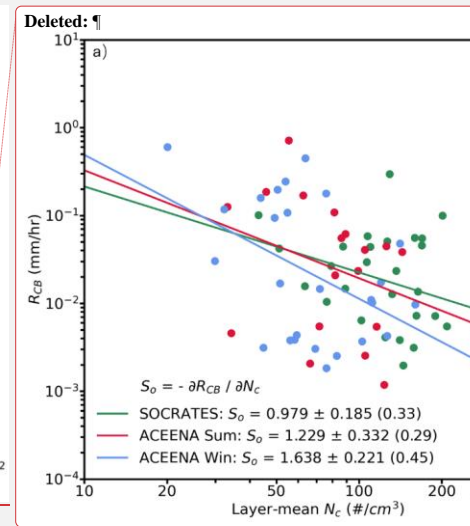
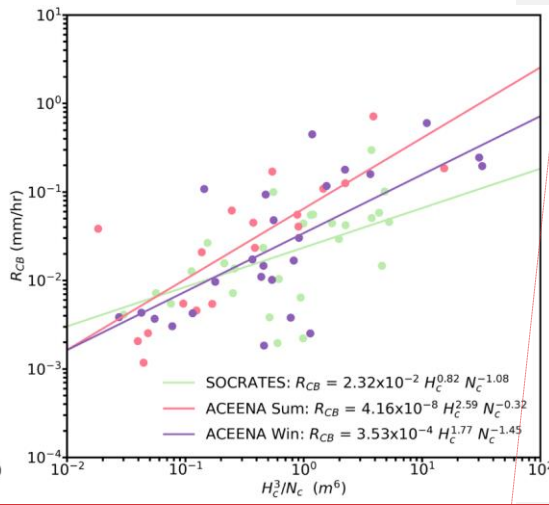
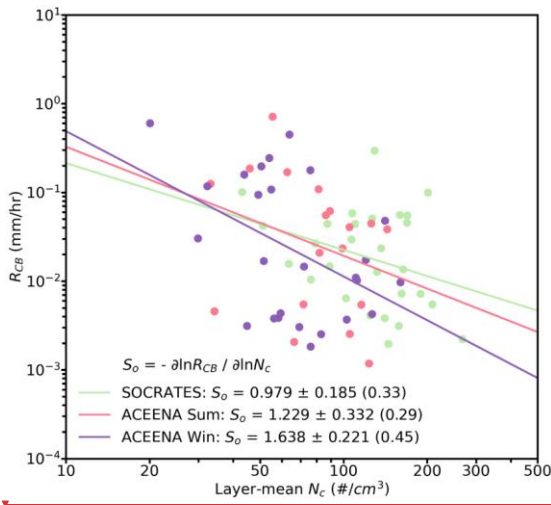


Figure 7. Scatterplots of the cloud base precipitation rate R_{CB} against the a) layer-mean N_c and b) H_c^3/N_c . ACE-ENA summer, winter and SOCRATES are color-coded with pink, purple and green, respectively.

Deleted: red, blue

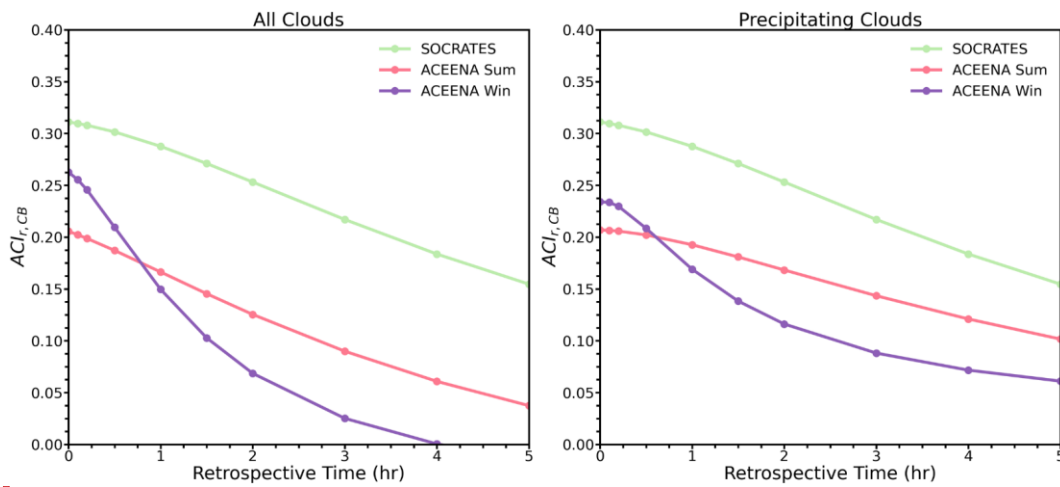
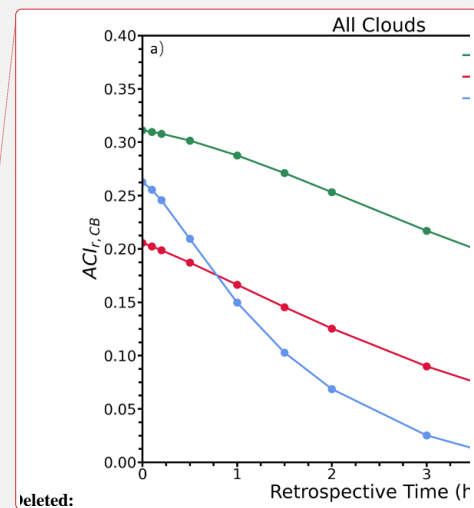


Figure 8. $ACI_{r,CB}$ as a function of the sub-cloud $N_{CCN0.35\%}$ retrospective time for a) all clouds and b) precipitating clouds.



releted: